Mechanical Systems and Signal Processing 230 (2025) 112602

Contents lists available at ScienceDirect

Mechanical Systems and Signal Processing

journal homepage: www.elsevier.com/locate/ymssp

Full Length Article

Isotactic and syndiotactic chiral mechanical metamaterials with tunable band gaps

Dewen Yu [a,b], Gang Wang [b], Qiangqiang Zhao [b,*], Wei Ding [c], Guobiao Hu [d,*], Jun Hong [b]

[a] Frontier Institute of Science and Technology, Xi'an Jiaotong University, Xi'an 710049, China
[b] Key Laboratory of Education Ministry for Modern Design and Rotor-Bearing System, School of Mechanical Engineering, Xi'an Jiaotong University, Xi'an 710049, China
[c] State Key Laboratory of Strength and Vibration of Mechanical Structures, School of Mechanical Engineering, Xi'an Jiaotong University, Xi'an 710049, China
[d] Internet of Things Thrust, The Hong Kong University of Science and Technology (Guangzhou), Guangzhou 511400, China

ARTICLE INFO

Keywords:
Chiral mechanical metamaterial
Tunable band gap
Wave propagation
Vibration suppression
Spectral element method

ABSTRACT

Although chiral mechanical metamaterials have garnered significant interest due to their wave manipulation capabilities, research into designs featuring adjustable dynamic characteristics remains relatively limited. This study presents an innovative design strategy that integrates adjustable rudder oscillators into periodic chiral lattices. A syndiotactic configuration is further proposed to produce multiple band gaps for broadband vibration suppression. Additionally, a programmable mechanism is introduced to actively regulate the band gap formation without compromising the structural integrity, particularly the static load-bearing capacity. To facilitate the analysis and optimization, a theoretical model that incorporates rigid-flexible and compressive-torsional coupling effects is developed to predict the transmittance spectra of such chiral metamaterials. For validation, both experiment tests and finite element simulations are conducted. The results obtained from all the means indicate that the syndiotactic configuration can produce vibration suppression zones over the ranges of 130.3–246.7 Hz, 293.4–369.0 Hz, and 597.7–995.6 Hz, while the isotactic one can only suppress vibrations in the ranges of 292.3–369.4 Hz and 699.1–783.0 Hz. The overall bandwidth of the vibration suppression zones generated by the syndiotactic configuration increases by 266.3 %. Meanwhile, a comprehensive analysis is also performed to uncover the underlying mechanisms behind the band gap formation. Furthermore, we demonstrate the tunability of the proposed chiral metamaterials in terms of vibration suppression capability. This work not only provides new insights into the exceptional dynamic behaviors of syndiotactic chiral metamaterials but also establishes solid methodological foundations for their analysis.

1. Introduction

Mechanical metamaterials [1–3], as an emerging class of engineered structures, exhibit extraordinary properties not found in natural substances [4,5]. Such properties include negative Poisson's ratio [6], ultrahigh strength-to-density ratio [7], zero thermal

* Corresponding authors.
E-mail addresses: qzhao21@xjtu.edu.cn (Q. Zhao), guobiaohu@hkust-gz.edu.cn (G. Hu).

https://doi.org/10.1016/j.ymssp.2025.112602
Received 4 December 2024; Received in revised form 8 March 2025; Accepted 15 March 2025
Available online 24 March 2025

expansion coefficient [8], and multi-stable states [3]. Particularly, the evolution of mechanical metamaterials has also provided new avenues for manipulating elastic waves [9,10]. The formation of frequency-independent band gaps effectively prohibits vibration propagation, leading to rapid attenuation throughout their transmission [11]. Compared with Bragg band gaps [12], locally resonant band gaps [13] are more suitable for low-frequency vibration attenuation [14]. Moreover, inertial amplification [15,16] contributes to the creation of broadband gaps in metamaterials at low subwavelength frequencies. In addition, quasi-zero stiffness [17–20] enables nonlinear passive vibration isolation at ultralow frequencies.

Over the past few decades, numerous mechanical metamaterials [21,22] have been meticulously designed to achieve specific vibration suppression performance. Yet, a common drawback of these structures is that once fabricated, their mechanical properties cannot be easily modified without complete reconstruction [23]. This lack of flexibility diminishes their adaptivity to various working conditions that necessitate adjustable dynamic behaviors [24]. In the literature, there are two main strategies for tailoring the band gap properties of mechanical metamaterial. One way is to modulate the intrinsic properties with stimuli-responsive materials [25], and the other is to change the geometric configurations [26]. When stimulated by heat, stress, or electromagnetic fields, smart materials such as shape memory polymers [27] and piezoelectric patches [28] will trigger the reconfiguration of these mechanical metamaterials. A typical example is the active mechanical metamaterial proposed by Montgomery et al. [29], which actively manipulates the band gaps by applying an external magnetic field. More recently, Dudek et al. [30] presented a magneto-mechanical metamaterial that allows for dramatic shape change, thereby empowering the tunability of phononic band gaps. In addition, mechanical loading-induced geometric deformations provide a robust means to modify both the position and width of band gaps. Following this concept, Wang et al. [31] investigated the effects of applied deformation on the low-frequency directionality of propagating waves. However, these active metamaterials not only require continuous loading [32] but also suffer the dilemma between broadband tunability and structural stability [33]. The second approach relies on changing the mass, size, or geometry of mechanical metamaterials [34]. For instance, Gu et al. [23] modulated the Dirac frequency of a honeycomb-lattice elastic metamaterial by adjusting the water depth of the cavities. Through theoretical modeling of the nonlinear dispersion relation for metamaterial beams, Shen and Lacarbonara [35] highlighted that a properly tuned softening resonator can significantly enlarge the stop band. Khosravi et al. [36] found that stretching kirigami sheets enables tuning band gaps for elastic waves at low frequencies. Through parametrical design, Wu et al. [37] changed the structural nonlinearity of X-shaped local resonators to adjust the bandgap width and location. Although these metamaterials achieve bandgap tuning over a broad frequency range, the reduction in the starting frequency and attenuation coefficient of the bandgap is inherently restricted by the structrual stiffness-to-mass ratio [38]. Hence, further exploration of novel techniques to decrease the bandgap frequency, while mataining the original mass and stiffness, is still actively pursued.

In such background, chirality-inspired periodic lattices have garnered significant attention for their fascinating tunable dynamic properties [39–41], such as elastic wave polarization [42] and the expansion of local resonance-induced bandgaps [43]. Making use of chiral internally resonating elements, the frequency-selective properties were integrated into lattice structures for low-frequency vibration control [44]. Zhu et al. [45] designed a chiral metamaterial beam with multiple resonators of individual bandgaps to enhance vibration suppression performance. By overlapping the flexural bandgap with the longitudinal-torsional bandgap, Park et al. [46] opened a complete bandgap in chiral trabeated metabeams. Zhang et al. [47] incorporated chiral local resonators into metamaterials to create a low-frequency bandgap with tunability. In essence, the widening of the local resonance-induced bandgap mainly benefits from the outstanding specific stiffness of chiral lattices. Yilmaz et al. [48] demonstrated that the translational-rotational coupling feature of chiral mechanical metamaterials endows the low-frequency band gaps with the inertial amplification effect. Bergamini et al. [38] and Zhao et al. [49] indicated that the dynamic properties of chiral lattice metamaterials are associated with tacticity. By changing the cascade form of chiral unit cells, the band gaps can be tuned without changing the relative density. In our previous studies [50,51], the analogy Thomson scattering was observed in planar chiral metamaterials. The results indicate that the initial frequency of attenuation can be comparable to the locally resonant band gap, whereas the bandwidth is remarkably broader. Although the wave propagation behaviors of purely chiral metamaterials have been well investigated, the formation mechanism of multiple bandgaps remains to be further explored for 3D chiral metamaterials with local resonators.

It is noteworthy that the accurate prediction of their transmittance spectra is a key prerequisite for the fine-tailoring of chiral mechanical metamaterials [52,53]. After all, mechanical testing is costly and time-consuming. At present, prevailing dynamic modeling approaches include the transfer matrix method (TMM) [54], the lumped mass-spring method (LMSM) [55], the plane wave expansion method (PWEM) [56], the finite element method (FEM) [57], and the spectral element method (SEM) [58]. Among these methods, the TMM struggles to model complex structures, limiting its application to one-dimensional systems [59]. Ding et al. [60,61] utilized LMSM to analyze the frequency response of chiral metamaterials, but the developed model demands a size-dependent correction factor to adjust the effective radius for accurate predictions. This correction may arise from the inherent discrepancy that the simplified discrete model cannot fully characterize the continuum structure in practical applications [62]. Regarding the PWEM, the material properties of the periodic medium are required to be expressed into a closed-form formula, thus reducing its versatility [63]. As adopted in [47,49,64,65], the calculation of the transmittance spectra of 3D chiral metamaterials still heavily relies on commercial FE software, but the simulation process is computationally demanding. In contrast to the FEM which necessitates fine meshes for precise solutions, the SEM enhances computational efficiency by using a single spectral element to model entire uniform segments [58,66,67]. However, due to the intricate nature of chiral metamaterials, including chiral branches and rigid bodies, no SEM has been presented to formulate the dynamic governing equations. Consequently, developing an efficient theoretical framework to predict the band gap properties of adjustable chiral metamaterials remains a significant challenge.

Motivated by the above research gaps, this study proposes and analyzes a novel type of chiral mechanical metamaterials with tunable band gaps. The main innovations of this work are threefold. (1) The developed chiral metamaterials with local resonators not only generate multiple band gaps below 1000 Hz but also offer high tunability and versatile configurations, allowing for the

customization of dynamic properties without sacrificing mass density and quasi-static stiffness. (2) An extended SEM model is developed that incorporates both rigid-flexible and compressive-torsional coupling effects within chiral mechanical metamaterials. This theoretical model enables direct prediction of vibration responses, facilitating efficient customization of band gaps without resorting to FE software or algorithm corrections. (3) Through the movement decomposition and edge eigenmodes, the wideband mechanism of syndiotactic configurations is revealed in compassion to isotactic configurations, providing new insights into the physics of elastic wave propagation in chiral metamaterials.

The rest of the paper is arranged as follows. Section 2 elucidates the structural design of the isotactic and syndiotactic chiral metamaterials with rudder oscillators. In Section 3, we develop a theoretical framework to reveal the band gap characteristics of such chiral metamaterials. Section 4 verifies the effectiveness of the theoretical model through both experimental and simulation results. Section 5 explores the wideband mechanism and tunable performance of such chiral metamaterials. Finally, the concluding remarks are provided in Section 6.

2. Structural design

Starting from the geometrical configurations, this section will introduce the design concept of a new type of mechanical metamaterial. Inspired by the concept of polymer chemistry [68], the isotactic and syndiotactic chiral mechanical metamaterials will be proposed in this section.

As illustrated in Fig. 1, the three-dimensional mechanical metamaterials are composed of chiral structures and rudder oscillators. The incorporation of chiral structures facilitates a coupling effect between torsional and compressive deformations, a behavior typically forbidden in conventional metamaterials due to symmetry constraints [39,41]. In addition, the inertial amplification effect inherent in the chiral structures contributes to the formation of broadband gaps at low frequencies [60,61]. Furthermore, the rudder oscillators are integrated to enhance the local resonator effects for this type of metamaterial, facilitating the creation of band gaps in the lower-frequency domain.

The topological configurations and geometric parameters of the chiral elementary cells are depicted in Fig. 1(a) and (b). Each chiral structure comprises two substrate plates with diameter d_p and height h_p. The adjacent substrate plates with a distance of h_c are connected vertically by three inclined beams. From the top view, these inclined beams are uniformly distributed along the perimeter of an enneagon, the circumscribed circle of which has a radius of r_1. The diameter and length of these inclined beams are defined by d_c and l_c, respectively. Moreover, as illustrated in Fig. 1(a), θ refers to the tilt angle between the inclined beams and the lower substrate plate. For the rudder oscillators, eight cantilever beams with a diameter of d_s extend from the upper substrate plate, and the attached mass blocks are of dimensions $l_m \times w_m \times h_m$. By introducing the screw-and-nut mechanism, the distance from each mass block to the center of the substrate plate is adjustable, denoted as r_2.

Within a chiral elementary cell, the inclined beams are grouped according to a specific rotational direction. Notably, the orientations of left- and right-handed chiral cells are not identical. The assembly strategy of these chiral elementary cells is inspired by the concept of "tacticity," a term originating from polymer chemistry. Tacticity refers to the specific arrangement of monomer units along the polymer chain and is primarily classified into two types: isotactic and syndiotactic. In isotactic polymers, the monomers are

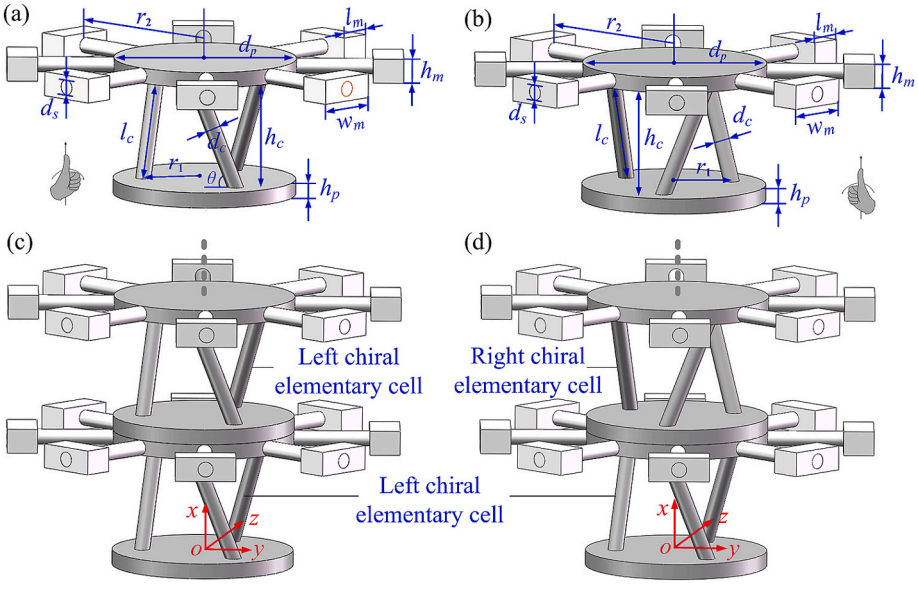

Fig. 1. Structural design of the chiral mechanical metamaterials. (a) Left chiral elementary cell; (b) Right chiral elementary cell; (c) Isotactic metamaterial with left chiral elementary cells periodically arranged; and (d) syndiotactic metamaterial with left and right chiral elementary cells alternately arranged.

arranged uniformly, whereas in syndiotactic polymers, they alternate in a regular pattern. Existing literature has shown that tacticity significantly affects the physical properties of polymers [69]. For example, while both isotactic and syndiotactic polypropylene are semicrystalline, they show significant differences in melting points, solubility, and mechanical strength [70]. It is worth noting that the elementary cells of metamaterial are analogous to the monomer units of the polymer. Moreover, the proposed two elementary cells exhibit similar structures, differing only in their chirality, which can be either left- or right-handed. Motivated by the intriguing characteristics of tacticity, we further design the isotactic and syndiotactic chiral metamaterials.

Specifically, when all rotational directions within a group are consistent, as illustrated in Fig. 1(c), the configuration is referred to as an "isotactic chiral metamaterial". When subjected to an external load along the x-axis, the deformation of the inclined beams triggers relative torsion between the upper and lower substrate plates. Given that all elementary cells in the isotactic arrangement share the same rotational direction, the resulting torsion accumulates perpendicularly to the substrate plates, inducing a tension–torsion coupling effect at the macroscopic scale. In contrast, the "syndiotactic chiral metamaterial" in Fig. 1(d) features an alternating arrangement of left- and right-handed chiral cells, effectively counteracting torsion due to the opposing rotational directions of neighboring cells.

3. Theoretical formulation

To elucidate the band gap properties of isotactic and syndiotactic chiral mechanical metamaterials, this section is dedicated to deriving the frequency response functions. Unlike the previous FE models that depend on commercial software, an extended spectral element method is developed to simultaneously account for both the rigid-flexible coupling effect and the compressive-torsional coupling effect within such chiral metamaterials.

3.1. Extended dynamic stiffness matrix for flexible beams

For describing the dynamic responses of the inclined beams and cantilever beams, a two-node spectral element with twelve degrees of freedom is constructed as depicted in Fig. 2. Considering the tensile, bending, and torsion deformations, the dynamic stiffness matrix $\mathbf{S}_b$ maps the nodal displacements $\mathbf{d}_{jk}$ to the corresponding nodal forces $\mathbf{F}_{jk}$ in the global coordinate system [58]:

$$\mathbf{S}_b\mathbf{d}_{jk} = \mathbf{F}_{jk} \tag{1}$$

Without loss of generality, as depicted in Fig. 2 (b), the vectors of nodal displacements $\mathbf{d}_{jk}$ and nodal forces $\mathbf{F}_{jk}$ for the n-th beam element are denoted by

$$\begin{cases} \mathbf{d}_{jk} = \left[\mathbf{d}_{n,j}^{\mathrm{T}}, \mathbf{d}_{n,k}^{\mathrm{T}}\right], \mathbf{d}_{n,j} = \left[u_j, v_j, w_j, \alpha_j, \beta_j, \gamma_j\right]^{\mathrm{T}}, \mathbf{d}_{n,k} = \left[u_k, v_k, w_k, \alpha_k, \beta_k, \gamma_k\right]^{\mathrm{T}} \\ \mathbf{F}_{jk} = \left[\mathbf{F}_{n,j}^{\mathrm{T}}, \mathbf{F}_{n,k}^{\mathrm{T}}\right], \mathbf{F}_{n,j} = \left[F_{xj}, F_{yj}, F_{zj}, M_{xj}, M_{yj}, M_{zj}\right]^{\mathrm{T}}, \mathbf{F}_{n,k} = \left[F_{xk}, F_{yk}, F_{zk}, M_{xk}, M_{yk}, M_{zk}\right]^{\mathrm{T}} \end{cases} \tag{2}$$

Regarding the frequency-dependent global dynamic stiffness matrix $\mathbf{S}_b$, its detailed expression can be found in our previous study [8,58].

For the proposed chiral metamaterials, the deformation of the substrate plates and mass blocks is significantly smaller than that of

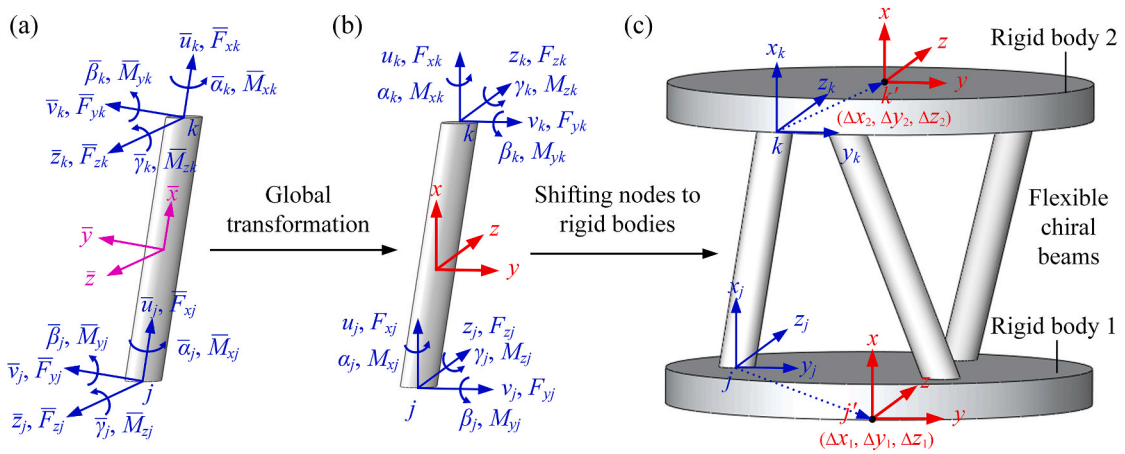

Fig. 2. Shifting the end nodes of a spatial flexible beam to the connected rigid bodies. Subplots (a) and (b) present a two-node spectral beam element in the local and global coordinate systems, respectively. Each node has six degrees of freedom, and the corresponding nodal forces include both translational and rotational components. Subplot (c) illustrates the shifting of the two nodes to the positions within the connected rigid bodies. The displacement vectors from j to j' and from k to k' are $(\Delta x_1, \Delta y_1, \Delta z_1)$ and $(\Delta x_2, \Delta y_2, \Delta z_2)$, respectively.

the beams, making it reasonable to treat the plates and blocks as rigid bodies within the focused frequency domain. Under this assumption, each end of the flexible beam is linked to a rigid substrate plate. Therefore, as illustrated in Fig. 2 (c), how to extend the spectral element method to formulate a flexible beam with its end nodes relocated to the positions of the connected rigid bodies becomes the central focus of theoretical modeling.

According to the transformational equations provided in Appendix A, the geometric and force relationship at nodes j and j' satisfies:

$$\mathbf{X}_{j'k} = \begin{bmatrix} \mathbf{I}_{3\times3} & \mathbf{0}_{3\times3} & \mathbf{0}_{3\times3} & \mathbf{0}_{3\times3} \\ \boldsymbol{\varpi}_1 & \mathbf{I}_{3\times3} & \mathbf{0}_{3\times3} & \mathbf{0}_{3\times3} \\ \mathbf{0}_{3\times3} & \mathbf{0}_{3\times3} & \mathbf{I}_{3\times3} & \mathbf{0}_{3\times3} \\ \mathbf{0}_{3\times3} & \mathbf{0}_{3\times3} & \mathbf{0}_{3\times3} & \mathbf{I}_{3\times3} \end{bmatrix} \mathbf{X}_{jk} = \mathbf{T}_1^{\mathrm{T}} \mathbf{X}_{jk}, \quad \mathbf{F}_{j'k} = \begin{bmatrix} \mathbf{I}_{3\times3} & \mathbf{0}_{3\times3} & \mathbf{0}_{3\times3} & \mathbf{0}_{3\times3} \\ \boldsymbol{\varpi}_1 & \mathbf{I}_{3\times3} & \mathbf{0}_{3\times3} & \mathbf{0}_{3\times3} \\ \mathbf{0}_{3\times3} & \mathbf{0}_{3\times3} & \mathbf{I}_{3\times3} & \mathbf{0}_{3\times3} \\ \mathbf{0}_{3\times3} & \mathbf{0}_{3\times3} & \mathbf{0}_{3\times3} & \mathbf{I}_{3\times3} \end{bmatrix} \mathbf{F}_{jk} = \mathbf{T}_1^{\mathrm{T}} \mathbf{F}_{jk} \tag{3}$$

where $\mathbf{I}_{3\times3}$ and $\mathbf{0}_{3\times3}$ are the 3×3 identity and zero matrices, respectively; and the coefficient matrix $\boldsymbol{\varpi}_1$ within $\mathbf{T}_1$ is determined by

$$\boldsymbol{\varpi}_1 = \begin{bmatrix} 0 & \Delta z_1 & -\Delta y_1 \\ -\Delta z_1 & 0 & \Delta x_1 \\ \Delta y_1 & -\Delta x_1 & 0 \end{bmatrix} \tag{4}$$

Here, the vector $(\Delta x_1, \Delta y_1, \Delta z_1)$ defined in the global coordinate system is the relative displacement from the end node j to the node j'.

By combining with Eqs. (2) and (3), the original dynamic stiffness matrix can be extended to characterize a spatial flexible beam with its end node j shifted into the position j', which is formulated as

$$\mathbf{F}_{j'k} = (\mathbf{T}_1^{\mathrm{T}} \mathbf{S}_b \mathbf{T}_1) \mathbf{X}_{j'k} \tag{5}$$

Similarly, the end node k can also be moved to node k' located at the rigid body 2, thus removing the node k from the dynamic stiffness matrix of the flexible beam. Analogous to Eq.(3), the propagation of displacement and force between nodes k and k' is expressed as:

$$\mathbf{X}_{j'k'} = \begin{bmatrix} \mathbf{I}_{3\times3} & \mathbf{0}_{3\times3} & \mathbf{0}_{3\times3} & \mathbf{0}_{3\times3} \\ \mathbf{0}_{3\times3} & \mathbf{I}_{3\times3} & \mathbf{0}_{3\times3} & \mathbf{0}_{3\times3} \\ \mathbf{0}_{3\times3} & \mathbf{0}_{3\times3} & \mathbf{I}_{3\times3} & \mathbf{0}_{3\times3} \\ \mathbf{0}_{3\times3} & \mathbf{0}_{3\times3} & \boldsymbol{\varpi}_2 & \mathbf{I}_{3\times3} \end{bmatrix} \mathbf{X}_{j'k} = \mathbf{T}_2^{\mathrm{T}} \mathbf{X}_{j'k}, \quad \mathbf{F}_{j'k'} = \begin{bmatrix} \mathbf{I}_{3\times3} & \mathbf{0}_{3\times3} & \mathbf{0}_{3\times3} & \mathbf{0}_{3\times3} \\ \mathbf{0}_{3\times3} & \mathbf{I}_{3\times3} & \mathbf{0}_{3\times3} & \mathbf{0}_{3\times3} \\ \mathbf{0}_{3\times3} & \mathbf{0}_{3\times3} & \mathbf{I}_{3\times3} & \mathbf{0}_{3\times3} \\ \mathbf{0}_{3\times3} & \mathbf{0}_{3\times3} & \boldsymbol{\varpi}_2 & \mathbf{I}_{3\times3} \end{bmatrix} \mathbf{F}_{j'k} = \mathbf{T}_2^{\mathrm{T}} \mathbf{F}_{j'k}, \tag{6}$$

where the transfer matrix $\boldsymbol{\varpi}_2$ within $\mathbf{T}_2$ is given by

$$\boldsymbol{\varpi}_2 = \begin{bmatrix} 0 & \Delta z_2 & -\Delta y_2 \\ -\Delta z_2 & 0 & \Delta x_2 \\ \Delta y_2 & -\Delta x_2 & 0 \end{bmatrix} \tag{7}$$

The vector $(\Delta x_2, \Delta y_2, \Delta z_2)$ is the relative displacement from the end node k to the node k'.

As a result, the frequency-dependent dynamic response function between the nodal forces and displacements at nodes j' and k' can be established by integrating Eqs. (3) and (6) as follows:

$$\mathbf{F}_{j'k'} = \left[(\mathbf{T}_1 \mathbf{T}_2)^{\mathrm{T}} \mathbf{S}_b (\mathbf{T}_1 \mathbf{T}_2) \right] \mathbf{X}_{j'k'} = \left[\mathbf{T}^{\mathrm{T}} \mathbf{S}_b \mathbf{T} \right] \mathbf{X}_{j'k'} = \mathbf{D}_n \mathbf{X}_{j'k'} \tag{8}$$

where $\mathbf{D}_n$ is the global matrix for the inclined beam with its two end nodes shifted into the connected rigid bodies.

To facilitate the subsequent assembly of the global matrice of the entire chiral metamaterial, the dynamic relationship of the n-th element can be restructured into a one-to-one mapping form:

$$\begin{bmatrix} \mathbf{F}_{n,j'} \\ \mathbf{F}_{n,k'} \end{bmatrix} = \mathbf{D}_n \begin{bmatrix} \mathbf{X}_{n,j'} \\ \mathbf{X}_{n,k'} \end{bmatrix} = \begin{bmatrix} \mathbf{D}_{n,1} & \mathbf{D}_{n,2} \\ \mathbf{D}_{n,3} & \mathbf{D}_{n,4} \end{bmatrix} \begin{bmatrix} \mathbf{X}_{n,j'} \\ \mathbf{X}_{n,k'} \end{bmatrix} \tag{9}$$

Specifically, the displacement vectors at nodes j' and k' are denoted by $\mathbf{X}_{n,j'}$ and $\mathbf{X}_{n,k'}$, respectively, while the force vectors at these nodes are represented by $\mathbf{F}_{n,j'}$ and $\mathbf{F}_{n,k'}$, respectively. The sub-matrices $\mathbf{D}_{n,1}$, $\mathbf{D}_{n,2}$, $\mathbf{D}_{n,3}$, and $\mathbf{D}_{n,4}$ are the components of the extended dynamic stiffness matrix $\mathbf{D}_n$. All of these vectors and matrices are defined in the global coordinate system.

It is noteworthy that, although our previous work [58] addressed the spectral stiffness of flexible rectangular plates, applying this technique to model circular flexible plates within chiral metamaterials presents substantial challenges. First, the spectral element method generally adopts line nodes for characterizing plate elements. To achieve compatibility between the spectral stiffness matrices of the substrate plate and the chiral lattice structure, a transformation from arc-line nodes (instead of straight-line nodes) to point nodes is required. Second, unlike hourglass meta-structures which permit the discretization of substrate plates with rectangular plate elements, chiral metamaterials demand the use of both circular and annular plate elements. Additionally, these plate elements do not adhere to standard boundary conditions (such as clamped, Levy-type supported, or free edges), which inevitably increases the computational complexity.

In light of the structural properties of chiral metamaterials, the theoretical formulation presented here advances the extended dynamic stiffness matrix of flexible spectral elements that connect two rigid bodies. By appropriately introducing the rigid-flexible coupling assumption, this formulation effectively mitigates the complexity of modeling circular plates via the spectral element

method. As demonstrated in Section 4, the developed approach offers a highly efficient and accurate way to predict the vibrational response of such chiral metamaterials.

3.2. Dynamic frequency response of the entire structure

As depicted in Fig. 3, an elementary cell consists of 10 nodes. By incorporating the extended dynamic stiffness matrix into the force equilibrium equations (see Appendix B), the following expression is obtained:

$$\begin{cases} \text{Node 1}: \mathbf{F}_{\text{int}}(\omega) = (\mathbf{D}_{1,\ 1} + \mathbf{M}_p)\boldsymbol{x}_1 + \mathbf{D}_{1,\ 2}\boldsymbol{x}_2 \\ \text{Node 2}: \mathbf{F}_{\text{out}}(\omega) = \mathbf{D}_{1,\ 3}\boldsymbol{x}_1 + (\mathbf{D}_{1,\ 4} + \mathbf{M}_p + \sum_{a=2}^{9}\mathbf{D}_{a,\ 1})\boldsymbol{x}_2 + \sum_{a=2}^{9}\mathbf{D}_{a,\ 2}\boldsymbol{x}_{a+1} \\ \text{Node 3}: \mathbf{0}_{6\times1} = \mathbf{D}_{2,\ 3}\boldsymbol{x}_2 + (\mathbf{D}_{2,\ 4} + \mathbf{M}_b)\boldsymbol{x}_3 \\ \text{Node 4}: \mathbf{0}_{6\times1} = \mathbf{D}_{3,\ 3}\boldsymbol{x}_2 + (\mathbf{D}_{3,\ 4} + \mathbf{M}_b)\boldsymbol{x}_4 \\ \quad , \ \cdots \\ \text{Node 9}: \mathbf{0}_{6\times1} = \mathbf{D}_{8,\ 3}\boldsymbol{x}_2 + (\mathbf{D}_{8,\ 4} + \mathbf{M}_b)\boldsymbol{x}_9 \\ \text{Node 10}: \mathbf{0}_{6\times1} = \mathbf{D}_{9,\ 3}\boldsymbol{x}_2 + (\mathbf{D}_{9,\ 4} + \mathbf{M}_b)\boldsymbol{x}_{10} \end{cases} \tag{10}$$

where $\mathbf{F}_{\text{int}}(\omega)$ and $\mathbf{F}_{\text{out}}(\omega)$ are the forces applying on the input and output ports, respectively; $\boldsymbol{x}_n$ is the nodal displacement vector of the n-th node. Specifically, the inertial matrices $\mathbf{M}_p$ and $\mathbf{M}_b$ are defined in Appendix B.

On this basis, the 3D dynamic stiffness model of the spatial chiral structure can be obtained by rewriting Eq.(10):

$$\left[\mathbf{F}_{\text{int}}^{\text{T}}(\omega), \mathbf{F}_{\text{out}}^{\text{T}}(\omega), \mathbf{0}_{1\times6}, \cdots, \mathbf{0}_{1\times6}, \mathbf{0}_{1\times6}, \mathbf{0}_{1\times6}\right]^{\text{T}} = \mathbf{D}_s\left[\boldsymbol{x}_1^{\text{T}}, \boldsymbol{x}_2^{\text{T}}, \boldsymbol{x}_3^{\text{T}}, \cdots, \boldsymbol{x}_7^{\text{T}}, \boldsymbol{x}_8^{\text{T}}, \boldsymbol{x}_9^{\text{T}}\right]^{\text{T}} \tag{11}$$

For conciseness, the expression for the dynamic stiffness matrix $\mathbf{D}_s$ of the elementary cell is provided in Appendix C.

After obtaining the condensed dynamic stiffness matrix of each unit cell, we can further predict the vibration response of the chiral structure, which can be simplified into a serial structure linked by rigid bodies. Subsequently, the boundary conditions are integrated into Eq.(11) to solve the response of the system. By using the extended dynamic stiffness matrix, the governing equation takes the form:

$$\begin{bmatrix} \mathbf{F}_{\text{int}}(\omega) \\ \mathbf{0}_{9\times6,1} \end{bmatrix} = \begin{bmatrix} \mathbf{D}_{\text{e}} & \mathbf{D}_{\text{ef}} \\ \mathbf{D}_{\text{ef}}^{\text{T}} & \mathbf{D}_{\text{f}} \end{bmatrix} \begin{bmatrix} \boldsymbol{x}_1 \\ \boldsymbol{x}_{\text{f}} \end{bmatrix} \tag{12}$$

where the subscripts ‘e’ and ‘f’ are short for “essential’’ and “free’’ boundary conditions, respectively. Therefore, the unknown variables can be solved as

$$\begin{cases} \boldsymbol{x}_{\text{f}} = -\mathbf{D}_{\text{f}}^{-1}\mathbf{D}_{\text{ef}}^{\text{T}}\boldsymbol{x}_1 \\ \mathbf{F}_{\text{int}} = (\mathbf{D}_{\text{e}} - \mathbf{D}_{\text{ef}}\mathbf{D}_{\text{f}}^{-1}\mathbf{D}_{\text{ef}}^{\text{T}})\boldsymbol{x}_1 \end{cases} \tag{13}$$

Based on the above formulation, the vibration transmittance of the chiral mechanical metamaterial is evaluated by

$$\psi(\omega) = 20\log\left(x_o/x_i\right) \tag{14}$$

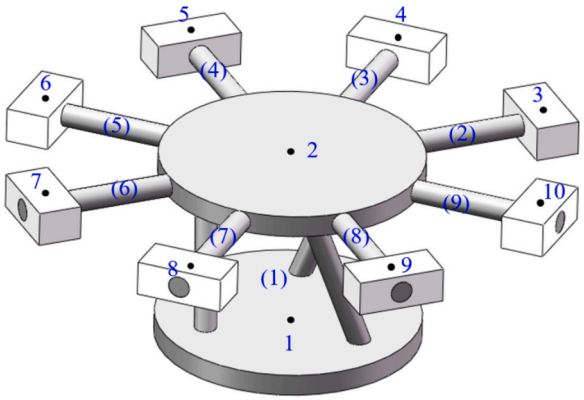

Fig. 3. Discretization and numbering of elementary cells. The numbers within the bracket stand for the index of mechanical parts or components, while the pure numbers without brackets represent the index of nodes. Nodes 1 and 2 are located at the geometric centers of the lower surface and upper surface of the substrate plates, respectively. The other nodes are fixed at the centers of mass blocks. After shifting the end nodes of inclined beams to substrate plates, the dynamic stiffness matrix of the chiral structure is condensed into a 12 × 12 matrix. Hence, the chiral structure is condensed into one component with two nodes.

where the vibration amplitudes x_i and x_o at the input and output ports can be extracted from the solution of Eq. (13). By definition, vibration attenuation occurs when $\psi(\omega) < 0$, which is also a necessary condition for the formation of a band gap.

3.3. Dispersion relation formulation for chiral metamaterials

As a well-established method, dispersion relation defines the relationship between wave frequency and wave number and is instrumental in identifying band gaps. Hence, this subsection focuses on deriving their dispersion relations to provide deeper insights into the band gap properties of isotactic and syndiotactic chiral metamaterials.

Drawing from previous studies on dispersion relation formulation [3,28,35], the first step is to construct the transfer matrix that relates the nodal displacements and forces at the input and output ports. In this regard, the dynamic relationship of an elementary cell, as presented in Eq. (11), is recast into

$$\begin{bmatrix} \mathbf{F}_{\text{int}} \\ \mathbf{F}_{\text{out}} \\ \mathbf{0}_{9\times 6} \end{bmatrix} = \begin{bmatrix} \mathbf{D}_{\text{LL}} & \mathbf{D}_{\text{ML}} & \mathbf{D}_{\text{RL}} \\ \mathbf{D}_{\text{LM}} & \mathbf{D}_{\text{MM}} & \mathbf{D}_{\text{RM}} \\ \mathbf{D}_{\text{LR}} & \mathbf{D}_{\text{MR}} & \mathbf{D}_{\text{RR}} \end{bmatrix} \begin{bmatrix} \boldsymbol{x}_1 \\ \boldsymbol{x}_2 \\ \boldsymbol{x}_m \end{bmatrix} \tag{15}$$

where x_m denotes the displacement vector of the nodes, excluding the first two. Through elimination and substitution operations, we can obtain

$$\begin{bmatrix} \boldsymbol{x}_1 \\ \mathbf{F}_{\text{int}} \end{bmatrix} = \begin{bmatrix} -\mathbf{C}^{-1}\mathbf{D} & \mathbf{C}^{-1} \\ \mathbf{B} - \mathbf{A}\mathbf{C}^{-1}\mathbf{D} & \mathbf{A}\mathbf{C}^{-1} \end{bmatrix} \begin{bmatrix} \boldsymbol{x}_2 \\ \mathbf{F}_{\text{out}} \end{bmatrix} = \mathbf{T}_d \begin{bmatrix} \boldsymbol{x}_2 \\ \mathbf{F}_{\text{out}} \end{bmatrix} \tag{16}$$

The corresponding block matrices are defined as:

$$\begin{cases} \mathbf{A} = \mathbf{D}_{\text{LL}} - \mathbf{D}_{\text{RL}}\mathbf{D}_{\text{RR}}^{-1}\mathbf{D}_{\text{LR}} \\ \mathbf{B} = \mathbf{D}_{\text{ML}} - \mathbf{D}_{\text{RL}}\mathbf{D}_{\text{RR}}^{-1}\mathbf{D}_{\text{MR}} \\ \mathbf{C} = \mathbf{D}_{\text{LM}} - \mathbf{D}_{\text{RM}}\mathbf{D}_{\text{RR}}^{-1}\mathbf{D}_{\text{LR}} \\ \mathbf{D} = \mathbf{D}_{\text{MM}} - \mathbf{D}_{\text{RM}}\mathbf{D}_{\text{RR}}^{-1}\mathbf{D}_{\text{MR}} \end{cases} \tag{17}$$

Subsequently, the Bloch-Floquet periodic boundary condition is applied to derive the dispersion relation for the isotactic chiral metamaterial, which requires

$$\begin{bmatrix} \boldsymbol{x}_2 \\ \mathbf{F}_{\text{out}} \end{bmatrix} = e^{\mathrm{i}q(h_s+2h_p)} \begin{bmatrix} \mathbf{I}_{6\times 6} & \mathbf{0}_{6\times 6} \\ \mathbf{0}_{6\times 6} & \mathbf{I}_{6\times 6} \end{bmatrix} \begin{bmatrix} \boldsymbol{x}_1 \\ \mathbf{F}_{\text{int}} \end{bmatrix} \Leftrightarrow \begin{bmatrix} \boldsymbol{x}_1 \\ \mathbf{F}_{\text{int}} \end{bmatrix} = e^{-\mathrm{i}q(h_s+2h_p)} \mathbf{I}_{12\times 12} \begin{bmatrix} \boldsymbol{x}_2 \\ \mathbf{F}_{\text{out}} \end{bmatrix} \tag{18}$$

where $\mathrm{i} = \sqrt{-1}$ is the imaginary unit and q is the wavenumber. Comparing Eq. (16) and Eq. (18) yields a standard eigenvalue problem:

$$\left| \mathbf{T}_d - e^{-\mathrm{i}q(h_s+2h_p)} \mathbf{I}_{12\times 12} \right| = 0 \tag{19}$$

Similar procedures can be applied to derive the dispersion relation of syndiotactic chiral metamaterials. It is worth noting that although the representative unit cell of the syndiotactic chiral metamaterial consists of two elementary cells, the internal nodes and forces can be condensed, allowing the final equation to be expressed in the same form as Eq. (16).

Solving Eq. (19) for a given ω yields the corresponding solution to wavenumber q. By sweeping ω and plotting the solved q, the band structures can be determined, leading to the identification of the band gap characteristics.

4. Experimental validation and simulation verification

In this section, the corresponding FE simulations and experimental measurements are provided to verify the theoretical formulation established in Section 3. The frequency responses and band structure of both isotactic and syndiotactic chiral metamaterials will be examined.

Table 1
Geometric parameters of the chiral metamaterials (unit: mm).

Structural parameter	Symbol	Value	Structural parameter	Symbol	Value
Height of substrate plates	h_p	5	Length of mass blocks	l_m	10
Diameter of substrate plates	d_p	60	Width of mass blocks	w_m	8
Height of inclined beams	h_c	35	Height of mass blocks	h_m	20
Length of inclined beams	l_c	37.58	Diameter of cantilever beams	d_s	5
Diameter of inclined beams	d_c	5	Length of cantilever beams	l_s	35
Circumscribed circle radius	r_1	20	Distribution radius of mass blocks	r_2	55

4.1. Examination of transmittance properties

Without loss of generality, the verification case study considers isotactic and syndiotactic chiral metamaterials consisting of 8 elementary cells along the *x*-direction. The structural parameters for both metamaterials are provided in Table 1, and the material properties of the resin used for all components are listed in Table 2.

In this case study, the transmittance spectra of the proposed metamaterials under harmonic excitation along the *x*-direction are computed using both SEM and FEM. The FE model is constructed with COMSOL Multiphysics® software. To experimentally validate the vibration suppression performance, prototypes of isotactic and syndiotactic chiral metamaterials are fabricated by 3D printing technology. The experimental setup, depicted in Fig. 4, involves suspending the prototype to simulate a free boundary condition. Excitation is generated at one end of the specimen using a shaker (The Modal Shop's Model 2060E), and the vibration transmission rate is measured with accelerometers (PCB 352C33) and a data acquisition system (ECON MI-7008).

Fig. 5 compares transmittance responses obtained from the developed theoretical model, the FE simulation, and the experimental measurement. It can be seen that the predicted transmittance aligns closely with those from both conventional FE simulations and experimental data. For the isotactic chiral metamaterial, two vibration suppression zones are identified in the frequency ranges of 292.3–369.4 Hz and 699.1–783.0 Hz, with normalized widths of $\Delta G_{i,1} = 0.233$, and $\Delta G_{i,2} = 0.113$, respectively. For the syndiotactic chiral metamaterial, three vibration suppression zones exist over the frequency ranges of 130.3–246.7 Hz, 293.4–369.0 Hz, and 597.7–995.6 Hz. The normalized widths are $\Delta G_{s,1} = 0.618$, $\Delta G_{s,2} = 0.228$, and $\Delta G_{s,3} = 0.499$, respectively.

On the one hand, the cumulative width of these band gaps for the syndiotactic chiral metamaterial covers 58.99 % of the frequency range below 1000 Hz, demonstrating superior broadband vibration suppression compared to [71]. On the other hand, these band gaps do not fall within the low-frequency domain typically sought for engineering applications. It is well-known that band gap formation strongly relies on the local resonators. Specifically, the band gap frequency could potentially be lowered by sacrificing the stiffness of the chiral metamaterial. However, such an investigation is beyond the scope of this study. Regarding low or ultra-low frequency vibration isolation, the metamaterials incorporating quasi-zero-stiffness isolators have shown promising application prospects. For more information, readers are encouraged to refer to [17–20], where the initial isolation frequency below 10 Hz is successfully achieved.

Throughout these vibration suppression regions, the relative errors between the theoretical predictions and FE simulations are below 3.62 % for the isotactic and 2.08 % for the syndiotactic metamaterials. In terms of computational performance, the theoretical model, implemented in Matlab on a desktop with a 3.40 GHz processor and 32 GB RAM, completes the frequency response analysis in an average of 5.67 s. In contrast, the FE simulation requires a significantly longer time, approximately 3.19×10^4 s. These results validate both the accuracy and computational efficiency of the proposed theoretical model for band gap analysis of chiral metamaterials.

A slight difference within the high-frequency region appears in the transmission spectrum of the isotactic configuration. This can be attributed to the distortion of the upper substrate plates under high-frequency vibrations, as illustrated in Fig. 6. Unlike the syndiotactic chiral metamaterial whose substrate plates retain their initial flat state, the upper substrate plates of the isotactic chiral metamaterial are distorted under high-frequency vibrations. Therefore, the rigid assumption is not strictly satisfied for the high-frequency vibration of isotactic chiral metamaterial. Nevertheless, the proposed theoretical model remains effective in identifying vibration suppression zones for such chiral metamaterials. In the field of mechanical metamaterials, the first few band gaps are generally of particular interest. Moreover, as demonstrated by both simulation and experimental results, the developed theoretical model offers reliable and efficient predictions of these band gaps.

4.2. Investigation of band gap behaviors

In this subsection, the band structures are examined to better understand the wave types in chiral metamaterials. Under the excitation condition applied in this study, only symmetric longitudinal (SL) modes can be activated, represented by red-colored branches in Fig. 7. In addition to COMSOL simulation results, theoretical solutions to the dispersion relation are also provided, marked by blue-point branches. The good agreement between the theoretical and simulation results verifies the derived formulation in predicting dispersion relations of isotactic and syndiotactic chiral metamaterials.

Regarding the wave propagation of SL modes in the proposed isotactic chiral metamaterial, a complete band gap, as highlighted in the aqua area of Fig. 7(a), is opened within the frequency of 292.3–369.4 Hz. For the syndiotactic chiral metamaterial, as presented in Fig. 7(b), two narrower band gaps appear at lower frequencies, while a wider band gap is observed at higher frequencies. The respective frequency ranges for these band gaps are 130.3–246.7 Hz, 293.4–369.0 Hz, and 597.7–995.6 Hz. These intervals are fully consistent with the transmittance spectrum results shown in Fig. 5.

A careful comparison between Fig. 7 and Fig. 5 reveals a noteworthy feature: the absence of a band gap within the frequency range of 699.1–783.0 Hz for the isotactic chiral metamaterial. This observation prompts the question of whether the identified vibration suppression region should be considered a band gap. To explore this issue further, we will examine the vibration suppression zone

Table 2
Material parameters of the chiral metamaterials.

Material parameter	Symbol	Value	Material parameter	Symbol	Value
Mass density	ρ	1160 kg/m^3	Poisson's ratio	μ	0.41
Young's modulus	E	2.51×10^9N/m^2	Shear modulus	G	8.90×10^8N/m^2

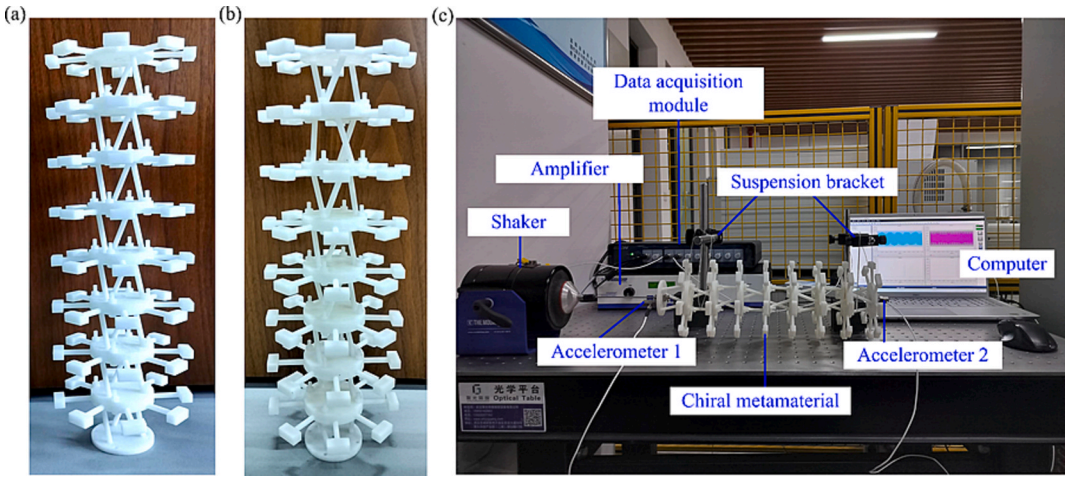

Fig. 4. Experiment verification on the vibration suppression performance. (a) Prototype of the isotactic chiral metamaterial; (b) Prototype of the syndiotactic chiral metamaterial. (c) Experimental measurement of vibration transmittance response.

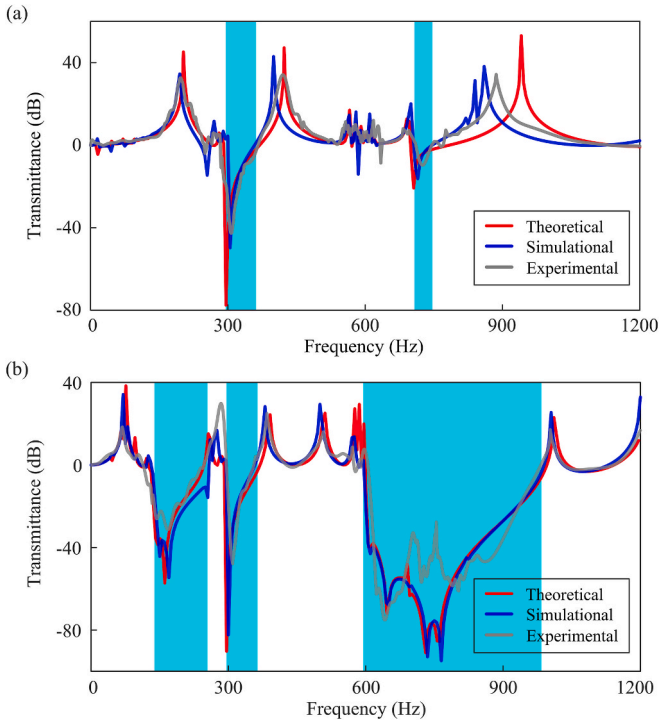

Fig. 5. Comparison of the transmission spectrums obtained by the theoretical prediction, FE simulation, and experimental test. (a) Transmission spectrum of the isotactic chiral metamaterial; (b) Transmission spectrum of the syndiotactic chiral metamaterial.

through two different perspectives, as detailed below.

On the one hand, it is well-established that the band gap in metamaterials often remains invariant with respect to the number of unit cells. For this reason, we analyze the transmittance spectra of three isotactic chiral metamaterials, each consisting of 6 to 10 elementary cells. As presented in Fig. 8, the first vibration suppression zone exhibits a constant width across all configurations. In contrast, the second vibration suppression zone narrows progressively as the number of elementary cells increases. On the other hand, Fig. 9 also illustrates the vibration modes corresponding to specific frequencies within the attenuation zones. Except for Fig. 9(b), where the response differs, all subplots reveal a consistent decay in vibration displacement along the x-direction. However, for the second vibration suppression zone of the isotactic chiral metamaterial, as shown in Fig. 9(b), the largest vibration displacement occurs at the output end, with the smallest displacement situated at the central cell. Notably, the vibration transmittance in this zone does not

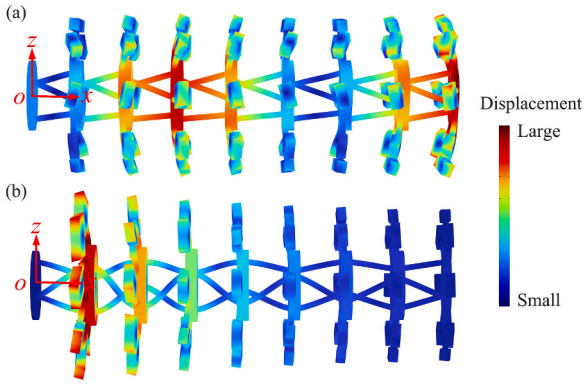

Fig. 6. Structural deformation at the resonant peak within the high-frequency zone. (a) Vibration mode of the isotactic chiral metamaterial at 861.4 Hz. (b) Vibration mode of the syndiotactic chiral metamaterial at 1005.1 Hz.

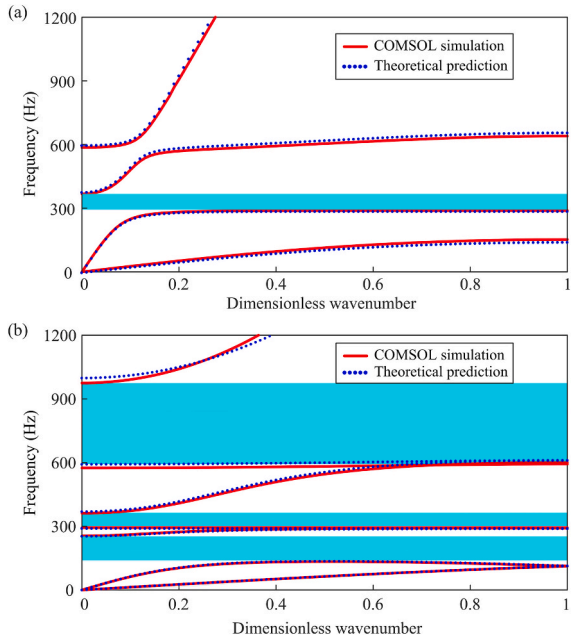

Fig. 7. Band structure of symmetric longitudinal mode for metamaterials. (a) and (b) are the band structures for the isotactic and syndiotactic chiral metamaterials, respectively. The band gaps are highlighted as aqua regions.

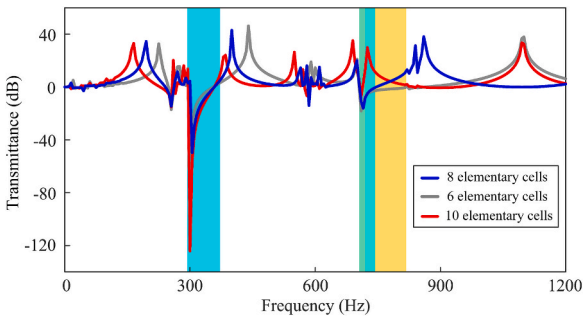

Fig. 8. Transmittance of the isotactic chiral metamaterials with different elementary cells. The width of the second vibration suppression zone gradually narrows with the increase of elementary cells, while that of the first zone is constant.

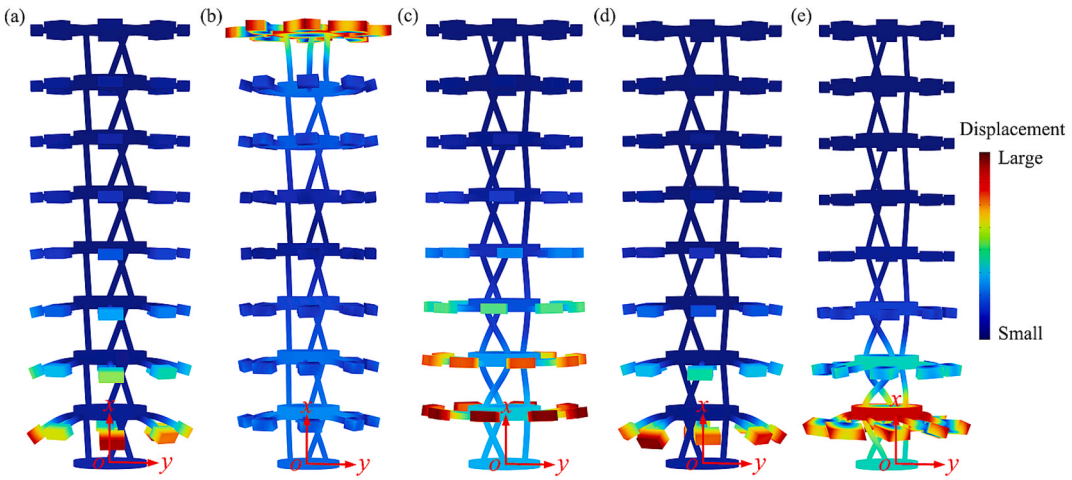

Fig. 9. Vibration transmittance modes of isotactic and syndiotactic chiral metamaterials within the vibration suppression zones. (a) and (b) are the vibration transmittance modes of the isotactic chiral metamaterial at the frequency of 310 Hz and 715 Hz, respectively. (c), (d), and (e) are the vibration transmittance modes of the syndiotactic chiral metamaterial at the frequency of 170 Hz, 305 Hz, and 705 Hz, respectively.

align with the typical properties of a band gap. As demonstrated above, the frequency range of 699.1–783.0 Hz should be classified as an ordinary vibration attenuation region rather than a genuine band gap for the isotactic chiral metamaterial.

5. Further discussion

After elucidating the band gap properties of chiral metamaterials, this section will provide a deep insight into the wideband mechanism of the syndiotactic chiral metamaterial. Moreover, we will discuss the tunability and programmability of the band gaps in such metamaterials, highlighting their potential for adaptive functionality.

5.1. Wideband mechanism of syndiotactic chiral metamaterials

As depicted in Fig. 5, the syndiotactic chiral metamaterial is capable of generating more and wider band gaps than the isotactic chiral metamaterial. However, Fig. 10 provides evidence that the transmittance spectra for the left- and right-handed chiral elementary cells are identical. What factors contribute to the differences in band gap characteristics between isotactic and syndiotactic chiral configurations? This subsection seeks to provide a comprehensive investigation into this intriguing phenomenon.

Firstly, we examine the frequency responses of the isostatic and syndiotactic chiral configurations, each comprising two elementary cells. As illustrated in Fig. 10, the first and fifth resonant peaks of the isostatic configuration occur at lower frequencies than those of the syndiotactic configuration, while the third resonant peak of the isostatic configuration appears at a higher frequency. In particular, the second and fourth resonant peaks of the isostatic configuration align in frequency with those of the syndiotactic configuration. This correspondence is primarily attributed to the same total mass and compression stiffness in both configurations. Moreover, the third vibration suppression region of the syndiotactic chiral configuration exhibits a broader span than that of the isostatic configuration. These findings suggest that the arrangement sequence of chiral metamaterials plays a critical role in determining their band gap

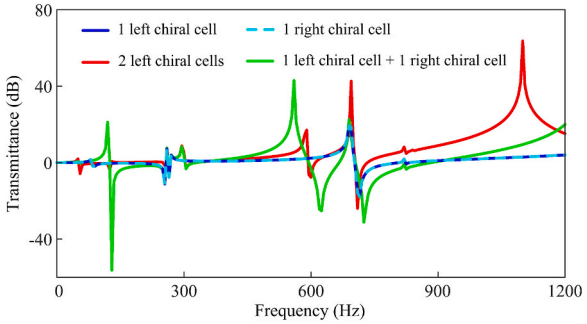

Fig. 10. Transmittance spectra of fundamental chiral metamaterials for longitudinal vibrations. Both left-handed and right-handed chiral elementary cells display identical transmittance spectra. In contrast, isostatic and syndiotactic chiral configurations, which incorporate two elementary cells, yield distinct vibrational responses.

characteristics.

The following discussion focuses on explaining the mechanism of wide bandgap generation. Fig. 11 shows the vibration orientations of oscillators during wave propagation in both isostatic and syndiotactic chiral structures. Initially, the vibration direction is along the x-axis with a phase of zero, leading to an incident wave that is excited in a translational manner. As the wave passes through the first elementary cell, the compressive-torsional coupling effect causes the translational displacement u_1 to divide into two components: the translation u_2 and the rotation φ_2. These components are subsequently scattered by the second elementary cell, generating four new waves: u_{31}, u_{32}, φ_{31}, and φ_{32}. Specifically, u_{31} and u_{32} are translational vibrations, while φ_{31} and φ_{32} are rotational vibrations.

In the case of the isostatic chiral configuration, the propagation direction of the scattered waves is depicted in Fig. 11(a). Initially, the translation component u_2 is along the $+x$ axis, and the rotation φ_2 rotates clockwise around the $+x$ axis. After the second scattering, considering u_2 as the incident wave, the scattered wave u_{31} propagates along the $+x$ axis, with the rotation φ_{31} rotating in a clockwise direction. Likewise, when φ_2 serves as the incident wave, the displacement wave u_{32} initially moves along the $+x$ axis, and φ_{32} also follows a clockwise rotation. Therefore, both translation components, u_{31} and u_{32}, as well as both rotational components, φ_{31} and φ_{32}, maintain a consistent orientation. Ultimately, the rotational angle φ_3 in the isostatic chiral configuration can be determined as

$$\varphi_3 = \varphi_{31} + \varphi_{32} = c(u_2 - u_{31}) + (\varphi_2 - cu_{32}) = c(u_2 - u_{31}) + [c(u_1 - u_2) - cu_{32}] = c(u_1 - u_3) \tag{20}$$

where c is the compressive-torsional coupling coefficient of each elementary unit.

For the syndiotactic chiral configuration, as depicted in Fig. 11(b), the scattered wave u_{31} propagates along the $+x$ axis, while the wave φ_{31} rotates in a clockwise direction. Meanwhile, the direction of u_{32} is reversed to the $-x$ axis, with φ_{32} rotating counterclockwise. As a result, the rotational angle φ_3 of the syndiotactic configuration is expressed as:

$$\varphi_3 = \varphi_{32} - \varphi_{31} = (\varphi_2 - cu_{32}) - c(u_2 - u_{31}) = [c(u_1 - u_2) - cu_{32}] - c(u_2 - u_{31}) = c(u_1 + u_3 - 2u_2) \tag{21}$$

As discussed above, the scattered waves vibrating in the same modes exhibit opposite vibration directions in a syndiotactic chiral configuration. Hence, the arrangement sequence directly affects the wave propagation behaviors of chiral metamaterials, thereby resulting in differences in the band gap formations.

Furthermore, band gap edge eigenmodes are provided to elucidate the formation mechanism of syndiotactic chiral metamaterials. Examining the modes at the edges of the band gap in the isostatic chiral metamaterial, as illustrated in Fig. 12(a) and (b), with particular attention to the upper bound edge mode in Fig. 12(b), reveals that the band gap observed in Fig. 7(a) arises from the translational local resonance of the rudder oscillators. The second to fourth-row subfigures in Fig. 12 serve to clarify the formation mechanism behind the three band gaps of the syndiotactic chiral metamaterial in Fig. 7(b). The modes depicted in Fig. 12(c) and (d) demonstrate that the rubber oscillators exhibit in-phase motions with the substrate plates to which they are attached. This indicates that the first band gap does not stem from the local resonance of the rubber oscillators for the syndiotactic chiral metamaterial. A comparison of the rotation directions of the three consecutive substrate plates, from bottom to top, reveals that phase inversion occurs alternately, leading to a destructive interference effect on wave propagation from one substrate plate to another. This phenomenon is observed in the syndiotactic chiral metamaterial but not in the isostatic counterpart because of the alternating chirality of adjacent cells within the syndiotactic chiral structure. The formation mechanism of the second band gap in the syndiotactic chiral metamaterial is elucidated in Fig. 12(e) and (f). Similar to the first band gap observed in the isostatic chiral metamaterial, the translational vibrations of the rudder oscillators are out of phase with the substrate plates to which they are affixed, resulting in a counteracting force that mitigates vibration. Concerning the third band gap of the syndiotactic chiral metamaterial, Fig. 12(g) and (h) illustrate that rotational modes predominantly govern the vibration of the entire structure over this frequency range. The in-plane vibrations of the rudder oscillators, which exhibit characteristics like rotation, effectively inhibit the clockwise vibrations of the substrate plates they attach to. Therefore, it can be concluded that the third band gap also arises from the local resonance mechanism of the rudder oscillators, albeit characterized by in-plane rotation-like resonance.

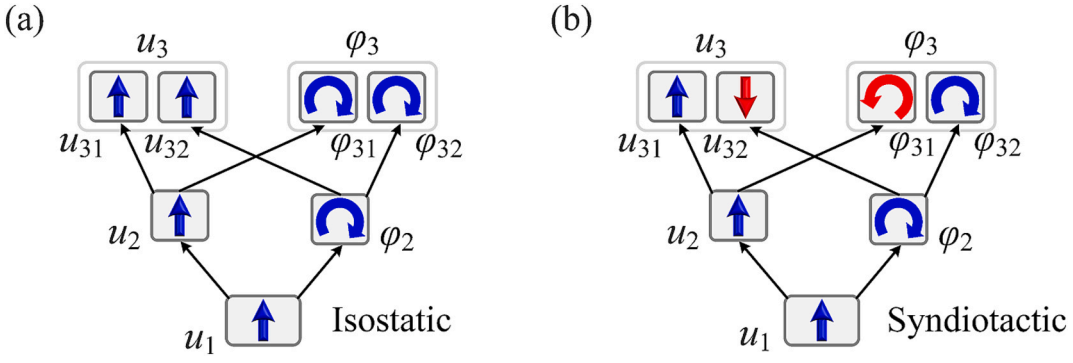

Fig. 11. Movement decomposition for (a) isostatic chiral configuration, and (b) syndiotactic chiral configuration. Due to the compressive-torsional coupling effect, both translational and rotational waves are scattered into two distinct components after passing through an elementary unit, with their propagation directions being affected by the tacticity.

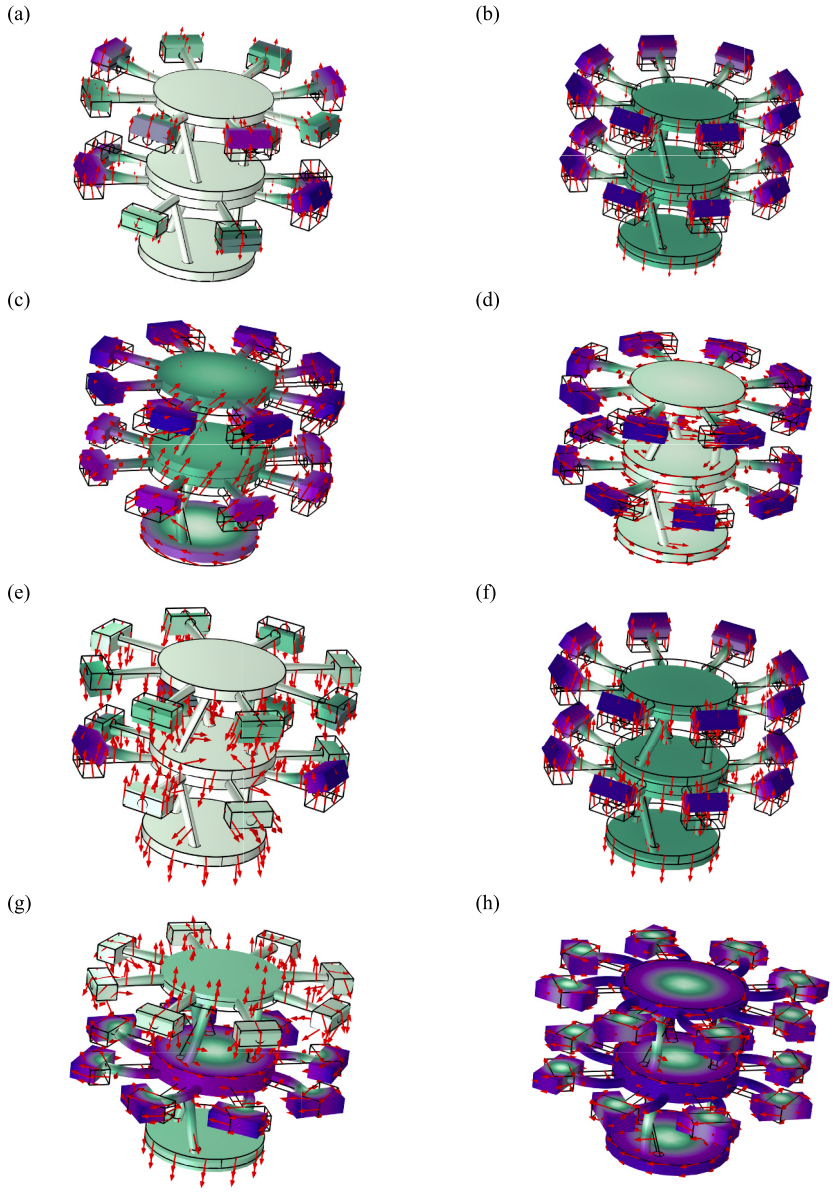

Fig. 12. Bandgap edge eigenmodes of the chiral metamaterials. (a) and (b) present the upper and lower edge modes of the band gap of the isostatic chiral metamaterial. (c) and (d) display the upper and lower edge modes of the first band gap of the syndiotactic chiral metamaterial. (e) and (f) demonstrate the upper and lower edge modes of the second band gap of the syndiotactic chiral metamaterial. (g) and (h) showcase the upper and lower edge modes of the third band gap of the syndiotactic chiral metamaterial.

5.2. Bandgap tunability of chiral metamaterials

As presented in the introduction, the band gaps of metamaterials are generally constrained by fixed vibrational properties, making them unsuitable for environments with fluctuating frequencies. For the metamaterials with tunable band gaps, they are primarily classified into two categories. One is empowered by smart materials like shape memory polymers to adapt to external loads, and the other is to modify the geometric configuration. The latter is often achieved at the sacrifice of structural integrity and load-bearing capacity. Especially for achieving band gaps within 1000 Hz, tunable metamaterials usually suffer from weak static strength.

For such chiral metamaterials, cantilever beams are structured as screws to adjust the distance r_2 between the mass blocks and the substrate plate. This structural design with the screw-and-nut mechanism facilitates the customization of band gaps, allowing them to be fine-tuned to meet the vibration suppression requirements of various engineering applications. As illustrated in Fig. 13, the main band gaps of both isotactic and syndiotactic chiral metamaterials shift to lower frequencies as r_2 increases. In the case of the syndiotactic chiral metamaterial at $r_2 = 35$ mm, the primary three band gaps occur in the frequency ranges of 159.8–479.2 Hz,

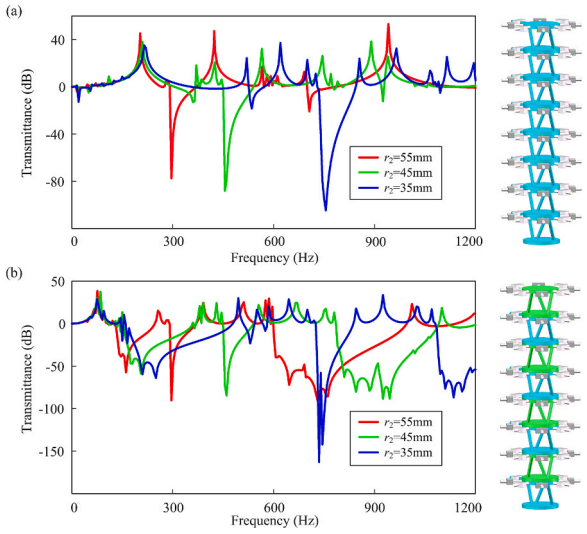

Fig. 13. Tunability of the band gaps for chiral metamaterials. (a) and (b) provide the dynamic responses of isotactic and syndiotactic chiral metamaterials, respectively. As depicted in the schematic diagrams on the right side, the distance (r_2) between the mass blocks and the substrate plated is adjustable, thereby achieving the programable band gaps.

725.4–837.9 Hz, and 1081.6–1248.1 Hz, with normalized widths of 0.997, 0.144, and 0.143, respectively. Compared to the syndiotactic configuration at $r_2 = 55$ mm, the first band gap widens, whereas the second and third band gaps narrow. Additionally, a new band gap appears within the frequency range of 507.5–543.7 Hz.

It is noteworthy that both the chiral direction and distance adjustment of elementary cells do not affect the load-bearing performance of the metamaterial. As demonstrated in Fig. 14, these configurations are of the same effective compression stiffness (209.38 N/mm). In particular, the total mass of the metamaterial remains constant throughout these adjustments. Therefore, such chiral metamaterials can achieve bandgap tunability without sacrificing their overall support stiffness and relative mass. Moreover, the equivalent strain resulting from a compressive force of 500 N for these configurations remains well within the failure strain limit (4.6 %) of the selected material, highlighting the effective load-bearing strength of the chiral metamaterials.

5.3. *Effects of tilt angle and boundary conditions*

In addition to the distance adjustment, the tilt angle and boundary conditions also have remarkable effects on the chiral metamaterials. As shown in Fig. 15, reducing the tilt angle, which enhances the structural chirality, leads to an expansion of the first and third band gaps. Moreover, for these two band gaps, their start frequencies shift downward, and cut-off frequencies move upward. Hence, if the material permits twisting, band gaps can also be manipulated effectively through shape morphing.

Furthermore, we observe that the constraints imposed on the unit cell also influence the band gap properties of the chiral metamaterials. As depicted in Fig. 16, two distinct types of constraints are applied to the substrate plates. Specifically, the “ON” status refers to applying a rotational constraint to the plates, while the “OFF” status indicates the unconstrained condition. The transmission profiles shown in Fig. 16 demonstrate that the rotational constraint significantly alters the band gap behaviors of the chiral metamaterials.

5.4. *Bandgap programmability of chiral structures*

More instrsteingly, the presence of both left- and right-handed chirality offers a versatile design strategy, while maintaining consistent relative density at the same time. By leveraging arbitrary coding techniques, it becomes possible to design a wide variety of 3D chiral mechanical metamaterials that integrate left- and right-chiral elementary units. Moreover, non-chiral elementary units can also be incorporated into the metamaterial design. These elementary units enable precise control over wave propagation within the 3D chiral mechanical metamaterial, allowing for the manipulation of chirality direction and the creation of tailored waveguides.

To further reveal the application potential of such chiral metamaterials, the effect of different code sequences on vibration suppression is assessed here. Similar to a binary coding scheme, the left- and right-chiral elementary units are assigned the values “1” and “2”, respectively, while the non-chiral unit is treated as “0”. By applying the concept of 3-bit configurations, there are 3^n possible configurations for a meta-structure consisting of n elementary units. Typically, metamaterials are periodic, but incorporating disorder into their design can provide enriched functionalities over ordered structures. These diverse combinations provide a wealth of options for achieving waveguide control over a wide range of frequencies.

As displayed in Fig. 17 (a), new metamaterials are constructed by switching the 3-bit configurations, which include periodic, mirror, and random arrangements. The corresponding transmittance spectra are shown in Fig. 17 (b). Among the configurations tested,

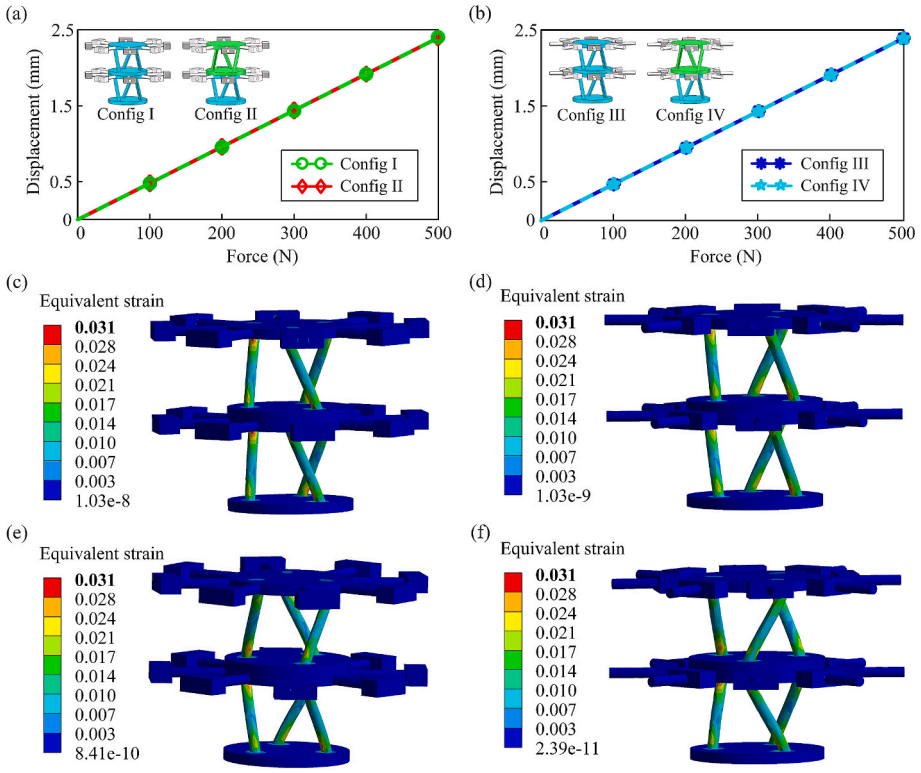

Fig. 14. Effective stiffness of different chiral metamaterials. (a) Displacement responses of syndiotactic and isotactic configurations with $r_2 = 55$ mm under compression; (b) Displacement responses of syndiotactic and isotactic configurations with $r_2 = 35$ mm under compression. These four configurations have the same effective compression stiffness of 209.38 N/mm. Subplots (c) and (d) illustrate the equivalent strain under a compression force of 500 N for isotactic configurations I and III, respectively. Similarly, (d) and (e) show the equivalent strain under the same compression force for syndiotactic configurations II and IV, respectively. The resulting maximum strain of these configurations is 3.1 %, which is lower than the failure strain (4.6 %) of the selected material.

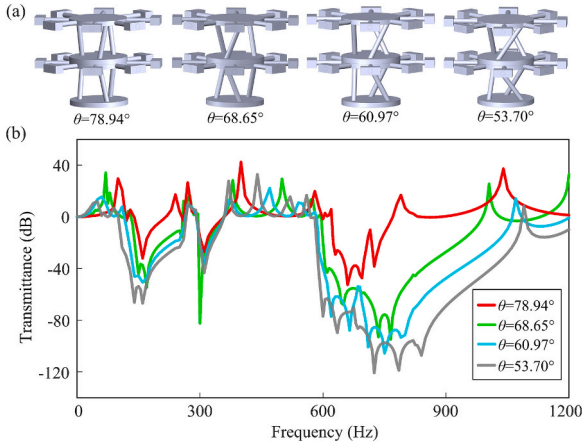

Fig. 15. Effects of the tilt angle on the transmittance spectra of syndiotactic chiral metamaterials. (a) Geometric configuration of the unit cells with various tilt angles for the chiral materials under investigation. (b) Bandgap characteristics of different syndiotactic chiral metamaterials with four unit cells.

the three chiral materials attributed to the inertial amplification [60,61] exhibit more vibration suppression regions than the non-chiral structure. In addition to the constant second attenuation region, variations in the code sequences alter both the width and the position of the band gaps. This clearly demonstrates that each configuration produces distinct band gaps, confirming the tunability and programmability of the bandgap properties in chiral metamaterials.

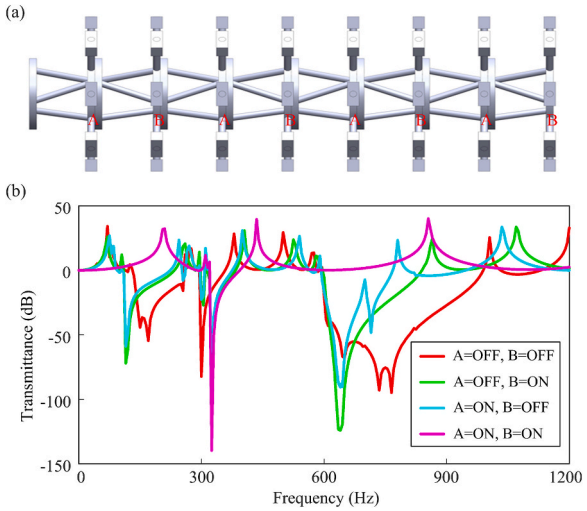

Fig. 16. Vibration responses of syndiotactic chiral metamaterials with different boundaries. (a) Illustration of the boundary condition; (b) Effects of boundary conditions on the transmittance spectra.

As discussed above, the diverse combinations of elementary cells allow for the development of various 3D chiral mechanical metamaterials, with coding sequences specifically tailored to achieve the desired vibration attenuation. Note that the developed theoretical framework is capable of accurately predicting the dynamic response of such metamaterials, thereby facilitating the foundation of a comprehensive data library linking topological configurations to performance outcomes. This advancement paves the way for applying machine learning techniques [72,73] to identify both optimal sequence and geometric parameters for targeted engineering applications, such as vibration suppression in deployable structures for spaceborne antennas [74,75].

6. Conclusion

In this work, a novel design strategy has been presented for developing chiral mechanical metamaterials with tunable band gaps. Based on thorough theoretical analyses and extensive technical discussions, the interesting observations and key findings are summarized below.

(1) By integrating adjustable rudder oscillators into chiral structures, the proposed mechanical metamaterials can achieve tunable band gaps within 1000 Hz, which are attributed to the coupling effects between the inherent inertial amplification and the incorporated local resonators.

(2) The results of FE simulations and experimental tests have proven that the developed theoretical model exhibits high accuracy and efficiency in predicting the dynamic response of such chiral mechanical metamaterials.

(3) The band structure analysis of chiral mechanical metamaterials reveals that the syndiotactic configuration generates more and broader band gaps owing to destructive interference. Interestingly, the second vibration attenuation region in the isotactic configuration is not a genuine band gap.

(4) Both adjustable rudder oscillators and programmable tacticity subsequences offer effective means of manipulating the band gaps of the chiral mechanical metamaterials without changing their overall weight, structural integrity, and load-bearing capacity.

In conclusion, this study provides valuable insights into the fundamental mechanisms behind the band gap formation in chiral mechanical metamaterials. Moreover, it establishes a reliable and highly efficient theoretical framework for the design and optimization of such tunable chiral metamaterials, thereby paving the way for promoting their practical applications in various engineering scenarios.

CRediT authorship contribution statement

Dewen Yu: Writing – review & editing, Writing – original draft, Validation, Investigation, Funding acquisition, Conceptualization. **Gang Wang:** Writing – original draft, Visualization, Validation, Software, Resources, Methodology, Data curation. **Qiangqiang Zhao:** Writing – original draft, Validation, Supervision, Resources, Methodology, Formal analysis, Conceptualization. **Wei Ding:** Methodology, Investigation, Formal analysis. **Guobiao Hu:** Writing – original draft, Visualization, Validation, Supervision, Methodology, Funding acquisition, Formal analysis. **Jun Hong:** Supervision, Resources, Project administration, Investigation, Formal analysis.

Declaration of competing interest

The authors declare that they have no known competing financial interests or personal relationships that could have appeared to

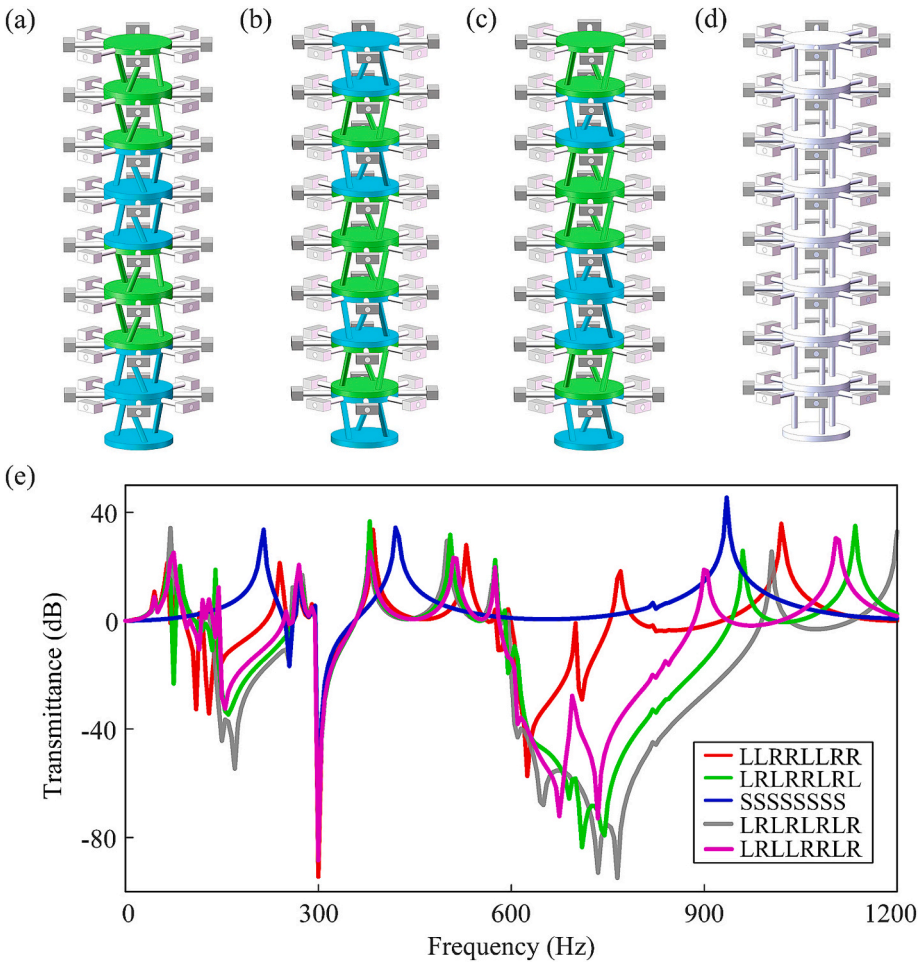

Fig. 17. Bandgap characteristics of different structures. For brevity, the letters "L", "R", and "S" are short for left chiral cell, right chiral cell, and straight cell (without chirality), respectively. The chiral structure (a) is with the combination of "LLRRLLRR" cells. The chiral structure (b) is composed of "LRLRRLRL" cells, which are symmetric with the upper surface of the fourth cell. The chiral elementary cells are randomly arranged to form the chiral structure (c), whose configuration is represented by "LRLRRLRL". For the structure (d), no chirality exists in its elementary cells, and this configuration is termed "SSSSSSSS". Taking the transmittance response of the syndiotactic chiral metamaterial (LRLRLRLR) as a benchmark, the subplot (e) depicts the variety of band gaps of the above structures.

influence the work reported in this paper.

Acknowledgments

The work is financially supported by the National Natural Science Foundation of China (Grant Nos. 52405291 & 52305135) and the Guangzhou Municipal Science and Technology Project (Grant No. 2023A03J0011). We would like to express our gratitude to Prof. Yaowen Yang from Nanyang Technological University for his valuable discussion.

Appendix A. . Geometric and force transformation relationships at shifted nodes

Based on the principles of solid mechanics, the geometric relationships and force equilibrium equations between nodes j and j' are derived as follows [67]:

$$\begin{cases} u_{j'} = u_j + \beta_j \Delta z_1 - \gamma_j \Delta y_1, & F_{xj'} = F_{xj} \\ v_{j'} = v_j - \alpha_j \Delta z_1 + \gamma_j \Delta x_1, & F_{yj'} = F_{yj} \\ w_{j'} = w_j + \alpha_j \Delta y_1 - \beta_j \Delta x_1, & F_{zj'} = F_{zj} \\ \alpha_{j'} = \alpha_j, & M_{xj'} = M_{xj} + F_{yj} \Delta z_1 - F_{zj'} \Delta y_1 \\ \beta_{j'} = \beta_j, & M_{yj'} = M_{yj} - F_{xj} \Delta z_1 + F_{zj} \Delta x_1 \\ \gamma_{j'} = \gamma_j, & M_{zj'} = M_{zj} + F_{xj} \Delta y_1 - F_{yj} \Delta x_1 \end{cases} \tag{A.1}$$

Here, the vector $(\Delta x_1, \Delta y_1, \Delta z_1)$ defined in the global coordinate system is the relative displacement from the end node j to the node j'.

Appendix B. . Dynamic equilibrium equations for an elementary cell

Following d'Alembert's principle, the forces acting on each node are equivalent to the sum of the reaction forces exerted by the connected flexible beams, the external forces, and the inertial forces inherent to the node. For an elementary cell, the principle yields the following sets of force equilibrium equations for the ten nodes:

$$\begin{cases} \text{Node 1}: \mathbf{F}_i(\omega) = \mathbf{F}_{1,j'} + \mathbf{M}_p \boldsymbol{x}_1 \\ \text{Node 2}: \mathbf{F}_o(\omega) = \mathbf{F}_{1,k'} + \mathbf{M}_p \boldsymbol{x}_2 + \sum_{a=2}^{9} \mathbf{F}_{a,j'} \\ \text{Node 3}: \mathbf{0}_{6\times1} = \mathbf{F}_{2,k'} + \mathbf{M}_b \boldsymbol{x}_3 \\ \text{Node 4}: \mathbf{0}_{6\times1} = \mathbf{F}_{3,k'} + \mathbf{M}_b \boldsymbol{x}_4 \\ \quad , \quad \cdots \\ \text{Node 9}: \mathbf{0}_{6\times1} = \mathbf{F}_{8,k'} + \mathbf{M}_b \boldsymbol{x}_8 \\ \text{Node 10}: \mathbf{0}_{6\times1} = \mathbf{F}_{9,k'} + \mathbf{M}_b \boldsymbol{x}_9 \end{cases} \tag{A.2}$$

where $\mathbf{F}_i(\omega)$ and $\mathbf{F}_o(\omega)$ are forces applying on the input and output ports, respectively; $\boldsymbol{x}_n$ is the nodal displacement vector of the n-th node; $\mathbf{M}_p$ and $\mathbf{M}_b$ are the inertial matrices of the substrate plate and the mass block, respectively. Taking the substrate plate as an example, its inertial matrix is determined by

$$\mathbf{M}_p = -\omega^2 \begin{bmatrix} \mathbf{M}_{3\times3} & \mathbf{0}_{3\times3} \\ \mathbf{0}_{3\times3} & \mathbf{J}_{3\times3} \end{bmatrix}, \mathbf{M}_{3\times3} = \begin{bmatrix} m_p & 0 & 0 \\ 0 & m_p & 0 \\ 0 & 0 & m_p \end{bmatrix}, \mathbf{J}_{3\times3} = \begin{bmatrix} J_x & 0 & 0 \\ 0 & J_y & 0 \\ 0 & 0 & J_z \end{bmatrix} \tag{A.3}$$

where m_p denotes the mass of the substrate plate; J_x, J_y, and J_z correspond to the mass moments of inertia about the coordinate axes at the geometric center of the upper surface of the substrate plate.

Appendix C. . Dynamic stiffness matrix of an elementary cell

According to Eq.(10), the dynamic stiffness matrix $\mathbf{D}_s$ of an elementary cell can be readily derived, and its expression is given by

$$\mathbf{D}_s = \begin{bmatrix} \mathbf{D}_{1,\,1} + \mathbf{M}_p & \mathbf{D}_{1,\,2} & \mathbf{0}_{6\times6} & \cdots & \mathbf{0}_{6\times6} & \mathbf{0}_{6\times6} & \mathbf{0}_{6\times6} \\ \mathbf{D}_{1,\,3} & \mathbf{D}_{1,\,4} + \mathbf{M}_p + \sum_{a=2}^{9} \mathbf{D}_{a,\,1} & \mathbf{D}_{2,\,2} & \cdots & \mathbf{D}_{7,\,2} & \mathbf{D}_{8,\,2} & \mathbf{D}_{9,\,2} \\ \mathbf{0}_{6\times6} & \mathbf{D}_{2,\,3} & \mathbf{D}_{2,\,4} + \mathbf{M}_b & \cdots & \mathbf{0}_{6\times6} & \mathbf{0}_{6\times6} & \mathbf{0}_{6\times6} \\ \vdots & \vdots & \vdots & \ddots & \vdots & \vdots & \vdots \\ \mathbf{0}_{6\times6} & \mathbf{D}_{7,\,3} & \mathbf{0}_{6\times6} & \cdots & \mathbf{D}_{7,\,4} + \mathbf{M}_b & \mathbf{0}_{6\times6} & \mathbf{0}_{6\times6} \\ \mathbf{0}_{6\times6} & \mathbf{D}_{8,\,3} & \mathbf{0}_{6\times6} & \cdots & \mathbf{0}_{6\times6} & \mathbf{D}_{8,\,4} + \mathbf{M}_b & \mathbf{0}_{6\times6} \\ \mathbf{0}_{6\times6} & \mathbf{D}_{9,\,3} & \mathbf{0}_{6\times6} & \cdots & \mathbf{0}_{6\times6} & \mathbf{0}_{6\times6} & \mathbf{D}_{9,\,4} + \mathbf{M}_b \end{bmatrix} \tag{A.4}$$

Data availability

No data was used for the research described in the article.

References

[1] P. Jiao, J. Mueller, J.R. Raney, X. Zheng, A.H. Alavi, Mechanical metamaterials and beyond, Nat. Commun. 14 (2023) 6004.
[2] M. Kadic, G.W. Milton, M. van Hecke, M. Wegener, 3D metamaterials, Nat. Rev. Phys. 1 (2019) 198–210.
[3] J. Ji, Q. Luo, K. Ye, Vibration control based metamaterials and origami structures: a state-of-the-art review, Mech. Syst. Sig. Process. 161 (2021) 107945.
[4] Y. Li, G. Yin, G. Yan, S. Yao, Forward-backstepping design of phononic crystals with anticipated band gap by data-driven method, Mech. Syst. Sig. Process. 224 (2025) 111975.
[5] T. Frenzel, M. Kadic, M. Wegener, Three-dimensional mechanical metamaterials with a twist, Science 358 (2017) 1072–1074.
[6] G. Wang, S. Wan, J. Hong, L. Li, S. Liu, X. Li, In plane mechanical properties of hexagonal V-chiral and Tri-chiral metamaterials, Eng. Struct. 315 (2024) 118502.
[7] J.U. Surjadi, L. Gao, H. Du, X. Li, X. Xiong, N.X. Fang, Y. Lu, Mechanical metamaterials and their engineering applications, Adv. Eng. Mater. 21 (2019) 1800864.
[8] D. Yu, G. Hu, W. Ding, Y. Yang, J. Hong, Zero-thermal-expansion metamaterial with broadband vibration suppression, Int. J. Mech. Sci. 258 (2023) 108590.

[9] H. Han, V. Sorokin, L. Tang, D. Cao, Origami-based tunable mechanical memory metamaterial for vibration attenuation, Mech. Syst. Sig. Process. 188 (2023) 110033.
[10] M. Sethi, A. Banerjee, B. Manna, Vibration transmission through a cantilever beam in mass impacting metamaterial: An analytical investigation and experimentation, Mech. Syst. Sig. Process. 220 (2024) 111669.
[11] A.O. Krushynska, M. Miniaci, F. Bosia, N.M. Pugno, Coupling local resonance with Bragg band gaps in single-phase mechanical metamaterials, Extreme Mech. Lett. 12 (2017) 30–36.
[12] Y. Ye, C. Mei, L. Li, X. Wang, L. Ling, Y. Hu, Broadening band gaps of Bragg scattering phononic crystal with graded supercell configuration, J. Vib. Acoust. 144 (2022) 061010.
[13] Z. Liu, X. Zhang, Y. Mao, Y.Y. Zhu, Z. Yang, C.T. Chan, P. Sheng, Locally resonant sonic materials, Science 289 (2000) 1734–1736.
[14] P.B. Lamas, R. Nicoletti, The spatial Fourier summation of corrugated beams and their band gap formation, Mech. Syst. Sig. Process. 215 (2024) 111396.
[15] C. Yilmaz, G. Hulbert, Theory of phononic gaps induced by inertial amplification in finite structures, Phys. Lett. A 374 (2010) 3576–3584.
[16] A. Banerjee, S. Adhikari, M.I. Hussein, Inertial amplification band-gap generation by coupling a levered mass with a locally resonant mass, Int. J. Mech. Sci. 207 (2021) 106630.
[17] S. Zuo, D. Wang, Y. Zhang, Q. Luo, Design and testing of a parabolic cam-roller quasi-zero-stiffness vibration isolator, Int. J. Mech. Sci. 220 (2022) 107146.
[18] Y. Lu, Q. Luo, L. Tong, Topology optimization for metastructures with quasi-zero stiffness and snap-through features, Comput. Methods Appl. Mech. Eng. 434 (2025) 117587.
[19] F. Zhao, J. Ji, S. Cao, K. Ye, Q. Luo, QZS isolators with multi-pairs of oblique bars for isolating ultralow frequency vibrations, Nonlinear Dyn. 112 (2024) 1815–1842.
[20] S. Zuo, D. Wang, Y. Zhang, Q. Luo, An innovative design of parabolic cam-roller quasi-zero-stiffness isolators for ultralow frequency vibration isolation, Nonlinear Dyn. 112 (2024) 18717–18744.
[21] S. Wan, L. Li, G. Wang, X. Li, J. Hong, A novel locally resonance metamaterial cylindrical shell with tower-shaped lattice for broadband vibration suppression, Mech. Syst. Sig. Process. 216 (2024) 111510.
[22] C. Cai, J. Zhou, K. Wang, H. Pan, D. Tan, D. Xu, G. Wen, Flexural wave attenuation by metamaterial beam with compliant quasi-zero-stiffness resonators, Mech. Syst. Sig. Process. 174 (2022) 109119.
[23] S. Ning, F. Yang, C. Luo, Z. Liu, Z. Zhuang, Low-frequency tunable locally resonant band gaps in acoustic metamaterials through large deformation, Extreme Mech. Lett. 35 (2020) 100623.
[24] P. Sinha, T. Mukhopadhyay, Programmable multi-physical mechanics of mechanical metamaterials, Mater. Sci. Eng. R. Rep. 155 (2023) 100745.
[25] Q. Wang, Z. Chen, Y. Wang, N. Gong, J. Yang, W. Li, S. Sun, A metamaterial isolator with tunable low frequency stop-band based on magnetorheological elastomer and magnet spring, Mech. Syst. Sig. Process. 208 (2024) 111029.
[26] P. Wang, F. Casadei, S.H. Kang, K. Bertoldi, Locally resonant band gaps in periodic beam lattices by tuning connectivity, Phys. Rev. B 91 (2015) 020103.
[27] Y. Wu, Y. Han, Z. Wei, Y. Xie, J. Yin, J. Qian, 4D printing of chiral mechanical metamaterials with modular programmability using shape memory polymer, Adv. Funct. Mater. 33 (2023) 2306442.
[28] G. Hu, L. Tang, Y. Yang, D. Yu, Y. Zi, High-fidelity dynamics of piezoelectric covered metamaterial timoshenko beams using the spectral element method, Smart Mater. Struct. 32 (2023) 095023.
[29] S.M. Montgomery, S. Wu, X. Kuang, C.D. Armstrong, C. Zemelka, Q. Ze, R. Zhang, R. Zhao, H.J. Qi, Magneto-mechanical metamaterials with widely tunable mechanical properties and acoustic bandgaps, Adv. Funct. Mater. 31 (2021) 2005319.
[30] K.K. Dudek, J.A. Iglesias Martínez, L. Hirsinger, M. Kadic, M. Devel, Active magneto-mechanical metamaterial with the wave transmission and Poisson's ratio controlled via the magnetic field, J. Sound Vib. 595 (2025) 118784.
[31] P. Wang, J. Shim, K. Bertoldi, Effects of geometric and material nonlinearities on tunable band gaps and low-frequency directionality of phononic crystals, Phys Rev B—Condens Matter Mater Phys 88 (2013) 014304.
[32] J. Wang, X. Liu, Q. Yang, R. Tao, Y. Li, L. Ma, A novel programmable composite metamaterial with tunable Poisson's ratio and bandgap based on multi-stable switching, Compos. Sci. Technol. 219 (2022) 109245.
[33] X. Fang, J. Wen, L. Cheng, D. Yu, H. Zhang, P. Gumbsch, Programmable gear-based mechanical metamaterials, Nat. Mater. 21 (2022) 869–876.
[34] S.-D. Zhao, A.-L. Chen, Y.-S. Wang, C. Zhang, Continuously tunable acoustic metasurface for transmitted wavefront modulation, Phys. Rev. Appl 10 (2018) 054066.
[35] Y. Shen, W. Lacarbonara, Nonlinear dispersion properties of metamaterial beams hosting nonlinear resonators and stop band optimization, Mech. Syst. Sig. Process. 187 (2023) 109920.
[36] H. Khosravi, S. Li, Tunable wave-propagation band gap via stretching kirigami sheets, Phys. Rev. Appl 17 (2022) 064054.
[37] Z. Wu, W. Liu, F. Li, C. Zhang, Band-gap property of a novel elastic metamaterial beam with X-shaped local resonators, Mech. Syst. Sig. Process. 134 (2019) 106357.
[38] A. Bergamini, M. Miniaci, T. Delpero, D. Tallarico, B. Van Damme, G. Hannema, I. Leibacher, A. Zemp, Tacticity in chiral phononic crystals, Nat. Commun. 10 (2019) 4525.
[39] I. Fernandez-Corbaton, C. Rockstuhl, P. Ziemke, P. Gumbsch, A. Albiez, R. Schwaiger, T. Frenzel, M. Kadic, M. Wegener, New twists of 3D chiral metamaterials, Adv. Mater. 31 (2019) 1807742.
[40] W. Wu, W. Hu, G. Qian, H. Liao, X. Xu, F. Berto, Mechanical design and multifunctional applications of chiral mechanical metamaterials: a review, Mater. Des. 180 (2019) 107950.
[41] H. Ou, L. Hu, Y. Wang, C. Liu, High-efficient and reusable impact mitigation metamaterial based on compression-torsion coupling mechanism, J. Mech. Phys. Solids 186 (2024) 105594.
[42] G. Carta, I. Jones, N. Movchan, A. Movchan, Wave polarization and dynamic degeneracy in a chiral elastic lattice, Proceedings of the Royal Society A 475 (2019) 20190313.
[43] A. Bacigalupo, G. Gnecco, M. Lepidi, L. Gambarotta, Optimal design of low-frequency band gaps in anti-tetrachiral lattice meta-materials, Compos. B Eng. 115 (2017) 341–359.
[44] E. Baravelli, M. Ruzzene, Internally resonating lattices for bandgap generation and low-frequency vibration control, J. Sound Vib. 332 (2013) 6562–6579.
[45] R. Zhu, X. Liu, G. Hu, C. Sun, G. Huang, A chiral elastic metamaterial beam for broadband vibration suppression, J. Sound Vib. 333 (2014) 2759–2773.
[46] J. Park, D. Lee, Y. Jang, A. Lee, J. Rho, Chiral trabeated metabeam for low-frequency multimode wave mitigation via dual-bandgap mechanism, Communications Physics 5 (2022) 194.
[47] R. Zhang, W. Ding, B. Fang, P. Feng, K. Wang, T. Chen, J. Zhu, Syndiotactic chiral metastructure with local resonance for low-frequency vibration isolation, Int. J. Mech. Sci. 281 (2024) 109564.
[48] A.H. Orta, C. Yilmaz, Inertial amplification induced phononic band gaps generated by a compliant axial to rotary motion conversion mechanism, J. Sound Vib. 439 (2019) 329–343.
[49] P. Zhao, K. Zhang, L. Qi, Z. Deng, 3D chiral mechanical metamaterial for tailored band gap and manipulation of vibration isolation, Mech. Syst. Sig. Process. 180 (2022) 109430.
[50] W. Ding, T. Chen, C. Chen, D. Chronopoulos, J. Zhu, B. Assouar, Thomson scattering-induced bandgap in planar chiral phononic crystals, Mech. Syst. Sig. Process. 186 (2023) 109922.
[51] W. Ding, T. Chen, D. Yu, C. Chen, R. Zhang, J. Zhu, B. Assouar, Isotacticity in chiral phononic crystals for low-frequency bandgap, Int. J. Mech. Sci. 261 (2024) 108678.
[52] H. Ronellenfitsch, N. Stoop, J. Yu, A. Forrow, J. Dunkel, Inverse design of discrete mechanical metamaterials, Phys. Rev. Mater. 3 (2019) 095201.
[53] J. Morris, W. Wang, D. Shah, T. Plaisted, C.J. Hansen, A.V. Amirkhizi, Expanding the design space and optimizing stop bands for mechanical metamaterials, Mater. Des. 216 (2022) 110510.

[54] Y. Li, H. Zhang, Theoretical analysis on topological interface states of 1D compression-torsion coupling metamaterial, Compos. Struct. 305 (2023) 116556.
[55] G. Hu, C. Lan, L. Tang, Y. Yang, Deep-subwavelength interface states in mechanical systems, Mech. Syst. Sig. Process. 169 (2022) 108598.
[56] C. Sugino, M. Ruzzene, A. Erturk, Merging mechanical and electromechanical bandgaps in locally resonant metamaterials and metastructures, J. Mech. Phys. Solids 116 (2018) 323–333.
[57] E. Nobrega, F. Gautier, A. Pelat, J. Dos Santos, Vibration band gaps for elastic metamaterial rods using wave finite element method, Mech. Syst. Sig. Process. 79 (2016) 192–202.
[58] D. Yu, G. Hu, Z. Guo, J. Hong, Y. Yang, Topological interface state formation in an hourglass lattice sandwich meta-structure, Int. J. Mech. Sci. 246 (2023) 108170.
[59] J. Zhang, X. Peng, D. Yu, G. Hu, Y. Yang, Rigid-elastic combined metamaterial beam with tunable band gaps for broadband vibration suppression, J. Vib. Acoust. (2024) 1–26.
[60] W. Ding, T. Chen, C. Chen, D. Chronopoulos, B. Assouar, Y. Wen, J. Zhu, Description of bandgaps opening in chiral phononic crystals by analogy with Thomson scattering, New J. Phys. 25 (2023) 103001.
[61] W. Ding, R. Zhang, T. Chen, S. Qu, D. Yu, L. Dong, J. Zhu, Y. Yang, B. Assouar, Origin and tuning of bandgap in chiral phononic crystals, Communications Physics 7 (2024) 272.
[62] Z. Deng, Y. Li, G. Gao, Bandgap tunability and programmability of four-leaf clover shaped elastic metastructures, Thin-Walled Struct. 200 (2024) 111965.
[63] V.F. Dal Poggetto, A.L. Serpa, Flexural wave band gaps in a ternary periodic metamaterial plate using the plane wave expansion method, J. Sound Vib. 495 (2021) 115909.
[64] J. Park, J. Noh, J. Shin, G.X. Gu, J. Rho, Investigating static and dynamic behaviors in 3D chiral mechanical metamaterials by disentangled generative models, Adv. Funct. Mater. 2412901 (2024).
[65] B. Lemkalli, M. Kadic, Y. El Badri, S. Guenneau, A. Mir, Y. Achaoui, The emergence of low-frequency dual Fano resonances in chiral twisting metamaterials, Wave Motion 127 (2024) 103302.
[66] G. Hu, A.C. Austin, V. Sorokin, L. Tang, Metamaterial beam with graded local resonators for broadband vibration suppression, Mech. Syst. Sig. Process. 146 (2021) 106982.
[67] M. Ling, D. Song, X. Zhang, X. He, H. Li, M. Wu, L. Cao, S. Lu, Analysis and design of spatial compliant mechanisms using a 3-D dynamic stiffness model, Mech. Mach. Theory 168 (2022) 104581.
[68] M. Huang, J. Chen, B. Wang, W. Huang, H. Chen, Y. Gao, T.J. Marks, Polar isotactic and syndiotactic polypropylenes by organozirconium-catalyzed masking-reagent-free propylene and amino–olefin copolymerization, Angew. Chem. 132 (2020) 20703–20709.
[69] Z. Zhou, A.M. LaPointe, G.W. Coates, Atactic, isotactic, and syndiotactic methylated polyhydroxybutyrates: an unexpected series of isomorphic polymers, J. Am. Chem. Soc. 145 (2023) 25983–25988.
[70] B.R. Paghadar, J. Sainani, P. Bhagavath, Internal donors on supported Ziegler Natta catalysts for isotactic polypropylene: a brief tutorial review, J. Polym. Res. 28 (2021) 1–19.
[71] H. Yang, S. Cheng, X. Li, Q. Yan, B. Wang, Y. Xin, Y. Sun, Q. Ding, H. Yan, Y. Li, Ultra-low-frequency multi-broadband and vibration suppression mechanism of innovative star-shaped hybrid metamaterials, Mater. Des. 230 (2023) 111966.
[72] C.S. Ha, D. Yao, Z. Xu, C. Liu, H. Liu, D. Elkins, M. Kile, V. Deshpande, Z. Kong, M. Bauchy, Rapid inverse design of metamaterials based on prescribed mechanical behavior through machine learning, Nat. Commun. 14 (2023) 5765.
[73] J. Kennedy, C. Lim, Machine learning and deep learning in phononic crystals and metamaterials – a review, Mater. Today Commun. 33 (2022) 104606.
[74] D. Yu, G. Hu, S. Cai, Y. Yang, J. Hong, Active optimization adjustment for the surface accuracy of spaceborne SAR antennas, Aerosp. Sci. Technol. 138 (2023) 108330.
[75] B. Siriguleng, W. Zhang, T. Liu, Y. Liu, Vibration modal experiments and modal interactions of a large space deployable antenna with carbon fiber material and ring-truss structure, Eng. Struct. 207 (2020) 109932.